



22 **Abstract**

23 Landslides present a significant hazard for humans, but continuous landslide  
24 monitoring is not yet possible due to their unpredictability. In recent years, numerical  
25 simulation and seismic inversion method have been used to provide valuable data  
26 for understanding the entire process of landslide movement. However, each method  
27 has shortcomings. Dynamic inversion based on long-period seismic signals gives the  
28 force-time history of landslide using empirical Green's function, but lack of detailed  
29 flowing characteristics of the hazards. Numerical simulation can simulate the entire  
30 movement process, but results are strongly influenced by choice of modelling  
31 parameters. Therefore, developing a method for combining those two techniques has  
32 become a focus for research in recent years. In this study, we develop such a protocol  
33 based on analysis of the 2018 Baige landslide in China. Seismic signal inversion  
34 results are used to constrain and optimize the numerical simulation. We apply the  
35 procedure to the Baige event and, combined with field/geological survey, show it  
36 provides a comprehensive and accurate method for dynamic process reconstruction.  
37 We found that the Baige landslide was triggered by detachment of the weathered  
38 layer, with severe top fault segmentation. The landslide process comprised four  
39 stages: initiation, main slip, blocking, and deposition. Multi-method mutual  
40 verification effectively reduces the inherent drawbacks of each method, and multi-  
41 method joint analysis improves the rationality and reliability of the results. The  
42 approach outlined in this study could help better understand the landslide dynamic

43 process.

44 ~~Landslides present a significant hazard for humans, but continuous landslide~~  
45 ~~monitoring is not yet possible due to their unpredictability. Post-event reconstruction~~  
46 ~~based on field survey and remote sensing cannot provide full insight into the~~  
47 ~~landslide movement process. Analysis and inversion of the seismic signals generated~~  
48 ~~by landslide movement has started to provide valuable data for understanding the~~  
49 ~~entire process of landslide movement, from initiation to cessation, along with~~  
50 ~~numerical simulation, but each method has shortcomings. Simple seismic signal~~  
51 ~~analysis can detect landslide occurrence, but the propagation effect generates lags.~~  
52 ~~Dynamic inversion based on long-period seismic signals gives the low-frequency~~  
53 ~~curve of landslide dynamic parameters, but not the high-frequency characteristics.~~  
54 ~~Numerical simulation can simulate the entire movement process, but results are~~  
55 ~~strongly influenced by choice of model parameters. Developing a method for~~  
56 ~~combining the three techniques has become a focus for research in recent years. Here,~~  
57 ~~we develop such a protocol based on analysis of the 2018 Baige landslide (China).~~  
58 ~~Seismic signal dynamic inversion results are used to verify the numerical simulation,~~  
59 ~~and then the numerical simulation is dynamically constrained and optimized to~~  
60 ~~obtain the best numerical simulationsvalue. We apply the procedure to the Baige~~  
61 ~~event and, combined with field/geological survey, show it provides a comprehensive~~  
62 ~~and accurate method for dynamic process reconstruction. We found that the Baige~~  
63 ~~landslide was triggered by detachment of the weathered layer, with severe top fault~~

64 ~~segmentation. The landslide process comprised four stages: initiation, main slip,~~  
65 ~~blocking, and deposition. Multi-method mutual verification effectively reduces the~~  
66 ~~inherent ambiguity of each method, and multi-method joint analysis improves the~~  
67 ~~rationality and reliability of the results. The approach outlined in this study could~~  
68 ~~help better understand the landslide dynamic process. The approach outlined in this~~  
69 ~~study could be used to support hazard prevention and control in sensitive areas.—~~

70 **Keywords:** Landslide processes reconstruction, Seismic signal analysis, Dynamic  
71 inversion, Numerical simulation, 2018 “10.10” Baige Landslide.

72

## 73 **1. Introduction**

74 Landslides present a significant hazard for humans, the number of fatalities resulting from  
75 non-coseismic landslides between 2004 and 2016 averaged 4,000 per year~~being responsible for~~  
76 ~~an average of 4,000 deaths per year between 2004 and 2016~~ (Froude and Petley, 2018). However,  
77 they cannot be continuously monitored due to their unpredictability and difficulty of detection  
78 (Chen et al., 2013; Yamada et al., 2013; Feng et al., 2016; Wang et al., 2020b), and the landslide  
79 movement process cannot be fully understood through post-event field investigation and remote  
80 sensing alone. Hence, to aid warning and prevention of landslide hazards and reduce associated  
81 losses, there is an urgent need to develop alternative methods to enable in-depth investigation of  
82 the dynamic characteristics of landslide generation and movement.

83 Landslide movement generates seismic signals that propagate to the surrounding area. The  
84 development of environmental seismology and construction of global seismic networks

85 (Dammeier et al., 2016) means the seismic signals generated by landslide movement can be  
86 quantitatively recorded by nearby seismic stations (Walter et al., 2012; Yamada et al., 2012; Chen  
87 et al., 2013; Yamada et al., 2013). Seismic signals generated by landslides reflect the duration,  
88 location, and scale of the event (Kao et al., 2012; Yamada et al., 2012; Chen et al., 2013); seismic  
89 signal analysis is increasingly used for landslide hazard monitoring and early warning, but it also  
90 offers a research tool for understanding landslide dynamics. The size and location of landslides  
91 can be estimated from the amplitude, frequency range, and time-frequency spectrum of the seismic  
92 signal (Favreau et al., 2010; Moretti et al., 2012; Moretti et al., 2015), along with timing of the  
93 event (Sakals et al., 2011; Zhang et al., 2019), and landslide dynamics (Yamada et al., 2013; Hibert  
94 et al., 2015; Jiang et al., 2016). The method of detecting, locating, and identifying landslide events  
95 using broadband seismograph records is based on associating seismic signals with landslide  
96 characteristics. Some progress has been made in interpreting landslide seismic signals, but signal  
97 recognition is often hindered by interference from seismic signals generated by other factors (Feng,  
98 2011; Zhao et al., 2015; Fuchs et al., 2018). Several methods have been developed to solve signal  
99 noise pollution (Helmstetter and Garambois, 2010; Feng, 2011), but analysis of landslide dynamic  
100 characteristics and reconstruction of landslide processes is still subject to errors and inaccuracies.  
101 Recently, filtering of seismic signals has been successfully applied to reconstruct dynamic  
102 landslide processes, allowing transition stages to be identified that are difficult to derive from field  
103 analysis alone (Yan et al., 2020a, 2020b).

104 Combining seismic signal analysis with dynamic inversion can improve the extraction of  
105 landslide dynamic characteristics. Landslide dynamic inversion using long-period seismic records

106 based on a single-force source model (Kanamori and Given, 1982; Kanamori et al., 1984;  
107 Hasegawa and Kanamori, 1987; Dahlen, 1993; Fukao, 1995) and a static point source assumption  
108 has been widely adopted to study landslide kinematics (Allstadt, 2013; Ekström and Stark, 2013;  
109 Yamada et al., 2013; Hibert et al., 2014, 2015; Moore et al., 2017; Gualtieri and Ekström, 2018;  
110 Li et al., 2019b; Sheng et al., 2020; Zhao et al., 2020). Predictive relationships between the  
111 maximum inverted forces and sliding volume can be derived from inverted landslide force histories  
112 (Ekström and Stark, 2013; Chao et al., 2016). Landslide basal friction is estimated directly using  
113 a block model (Brodsky et al., 2003; Allstadt, 2013; Yamada et al., 2013; Zhao et al., 2015; Yu et  
114 al., 2020) or obtained from seismic analysis coupled with numerical simulation (Moretti et al.,  
115 2012, 2015; Yamada et al., 2016, 2018). Although numerical simulation of landslide dynamic  
116 processes has achieved remarkable results, there are issues with each of the following three main  
117 approaches. ~~there are issues with each of the two main approaches.~~ The continuous medium  
118 approach, including smoothed particle hydrodynamics (SPH) (Pastor et al., 2014), material point  
119 method (MPM) (Soga et al., 2016), finite element method (FEM) (Muceku et al., 2016), finite  
120 volume method (FVM) (Pitman et al., 2003), and finite difference method (FDM) (Shen et al.,  
121 2020), is not very effective in describing particle separation and internal fracture of rockslides.  
122 The thin-layer models are based on the thin-layer approximation and depth-averaging of the  
123 Navier–Stokes equations without viscosity, but a main issue is low computational accuracy  
124 (Moretti et al., 2012, 2015; Yamada et al., 2016, 2018). The discrete element approach utilizes  
125 software such as particle flow code (PFC) (Lo et al., 2011; Zhang et al., 2020a) and DEM solutions  
126 (EDEM) (Wang et al., 2020c), but a major issue is low computational efficiency. The thin-layer

127 ~~model, it is based on the thin layer approximation and depth averaging of the Navier Stokes~~  
128 ~~equations without viscosity, but a main issues is low computational accuracy (Moretti et al., 2012,~~  
129 ~~2015; Yamada et al., 2016, 2018).~~ MatDEM uses an innovative matrix discrete element method  
130 and three-dimensional contact algorithm, which can realize the efficient numerical simulation of  
131 millions of particles (Liu et al., 2013, 2017). However, studies utilizing MatDEM mostly  
132 determine the correctness of landslide simulation through comparison with post-event landslide  
133 characteristics derived from field investigation (Liu et al., 2017), which may not represent dynamic  
134 processes. An alternative approach that offers potential is to use seismic signal inversion as the  
135 constraint on landslide dynamic process (Yamada et al., 2016, 2018).

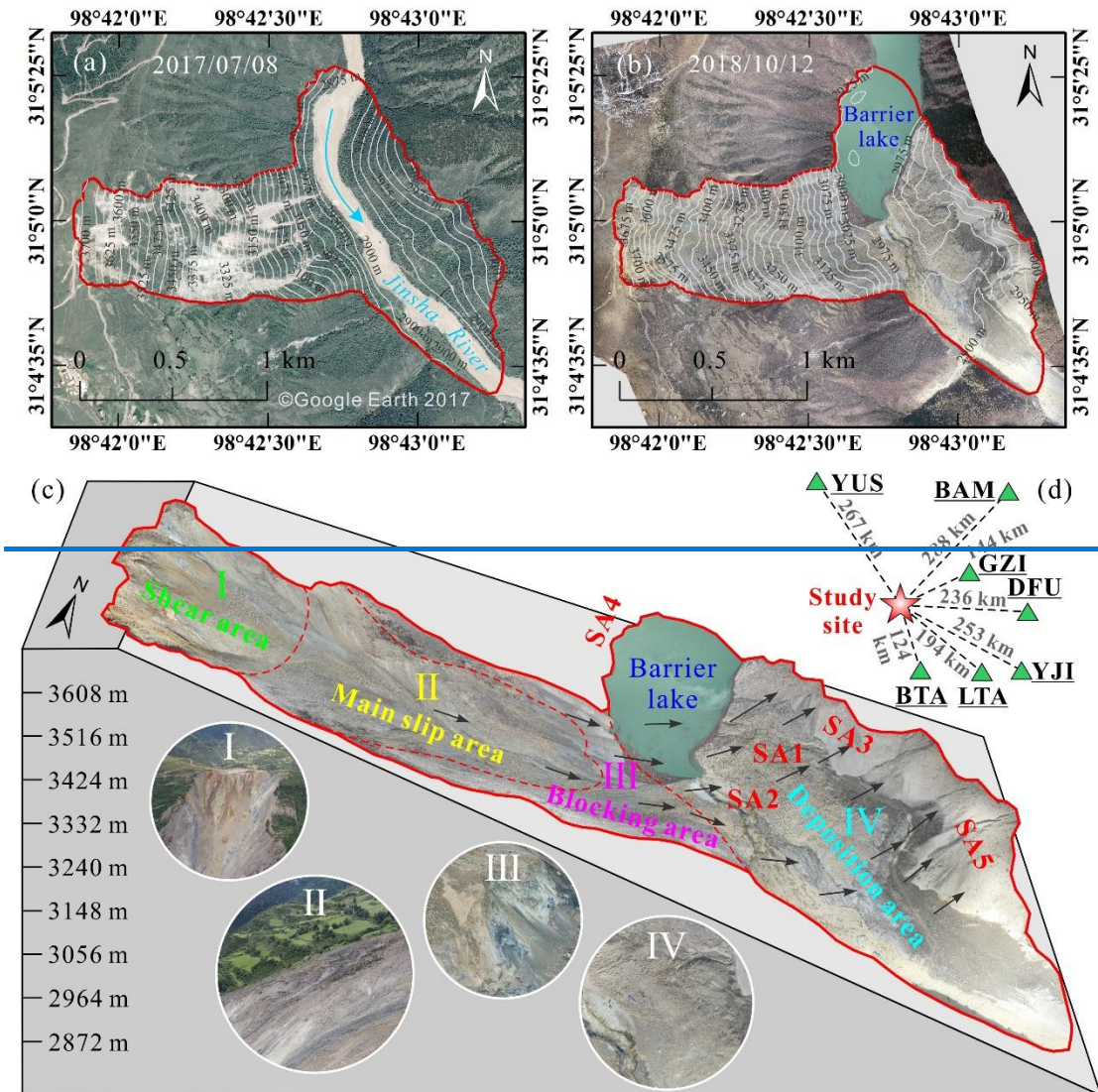
136 In this study, we use long period seismic signal to obtain the dynamic characteristics of Baige  
137 landslide, China, which occurred on October 10, 2018 (termed as the “10.10” event). Combined  
138 with the inversion results, the landslide process was reconstructed by numerical simulation.  
139 Through seismic signal analysis, landslide dynamic inversion and numerical simulation, combined  
140 with the post-event field investigation, By the dynamic inversion results by long period seismic  
141 signal which can be used to quality the landslide reconstruction using numerical simulation, and  
142 the post event field investigation and seismic signal analysis, we try to provide an improved  
143 characterization of the landslide movement process.~~In this study, we analyze the seismic signal of~~  
144 ~~Baige landslide, China, which occurred on October 10, 2018 (termed the “10.10” event) and obtain~~  
145 ~~the dynamic characteristics of the landslide by dynamic inversion. The inversion results are~~  
146 ~~compared with landslide reconstruction using numerical simulation combined with post event~~  
147 ~~field investigation, to provide an improved characterization of the landslide movement process.~~

148

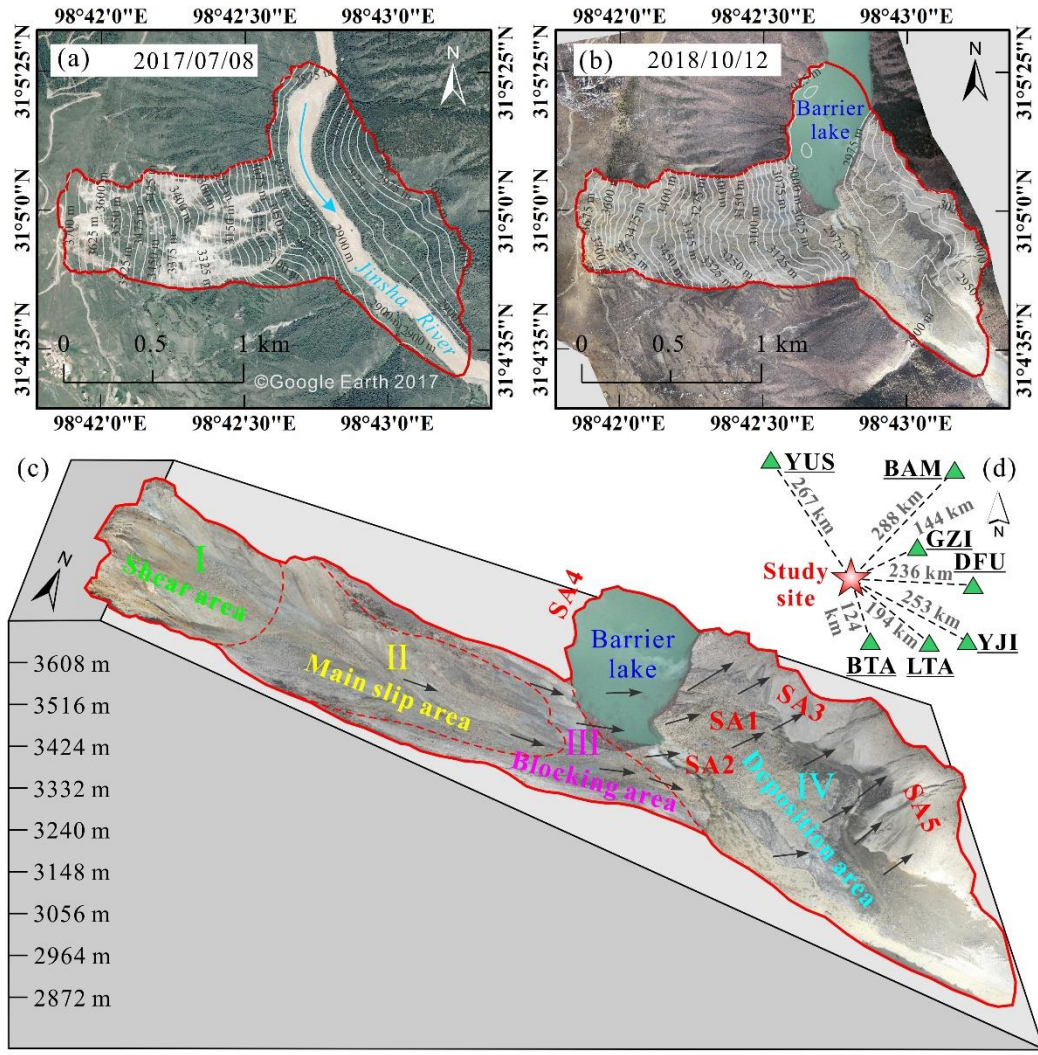
## 149 **2. Study area and data sources**

150 A massive landslide occurred at Baige, on the eastern Qinghai-Tibetan Plateau, China, on  
151 October 10, 2018— (termed as the “10.10” event) (Fig. 1). The landslide caused the blockage of  
152 the main stream of Jinsha River and formed a barrier lake. On October 12, the water of the barrier  
153 lake began to discharge naturally until all the discharge was completed on October 13. On  
154 November 3, 2018, the rock and soil mass at the trailing edge of the slide source area of the first  
155 Baige landslide was unstable again, causing the second landslide. It has been studied by many  
156 researchers, Xu et al. (2018) and Deng et al. (2019) analysed the formation mechanism and process  
157 of the landslide, and found that the site is in the Jinsha River suture zone, where the influence of  
158 multiple tectonic movements provides a complicated regional tectonic profile; the main fault  
159 structures trend NW, within the Jiangda-Bolo-Jinshajiang fault zone (Fig.2). Ouyang et al. (2019),  
160 Fan et al. (2019a) and Wang et al. (2020c) carried out numerical simulation analysis of Baige  
161 landslide. In this study, only the “10.10” Baige landslide was studied. ~~The site is in the Jinsha~~  
162 River suture zone, where the influence of multiple tectonic movements provides a complicated  
163 regional tectonic profile; the main fault structures trend NW, within the Jiangda Bolo Jinshajiang  
164 fault zone (Deng et al., 2019; Fan et al., 2019b; Xu et al., 2018) (Fig. 2). The landslide can be  
165 divided into four areas, namely, shear, main slip, blocking, and deposition, with maximum and  
166 average thicknesses of 80 and 50 m, ~~and thins to the sides~~ (Fig. 1c). We used terrain data from  
167 Ouyang et al. (2019), comprising a 10 m resolution pre-landslide Digital Elevation Model (DEM)  
168 from 2017, and a 5 m resolution post-slide DEM obtained through Unmanned Aerial Vehicle

169 [\(UAV\) photogrammetry in 2018 from field investigation](#). Based on [DEM](#) [Digital Elevation Model](#)  
 170 [\(DEM\)](#) differencing, total landslide volume was calculated as  $1.969 \times 10^4 \times 10^7 \text{ m}^3$ . [The altitude](#)  
 171 [range of the initiation zone is 3523 –to 3730 m](#). Most of the rock mass that collapsed from the steep  
 172 back wall accumulated at an elevation of 3100 –to 3300 m, in an area of gentle slope [angle from](#):-  
 173 20 –to 25°.

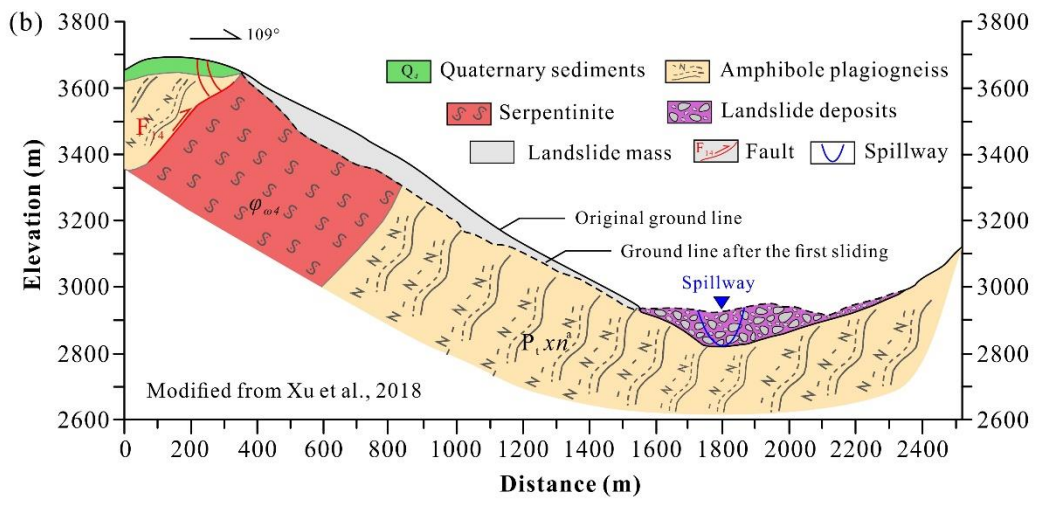
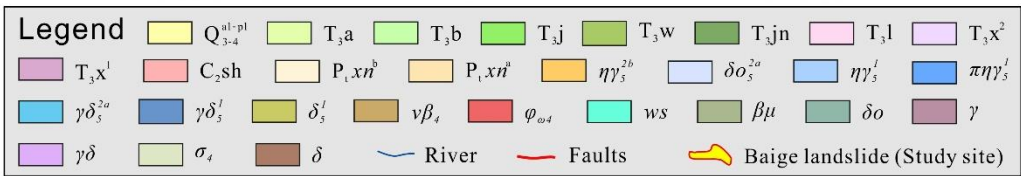
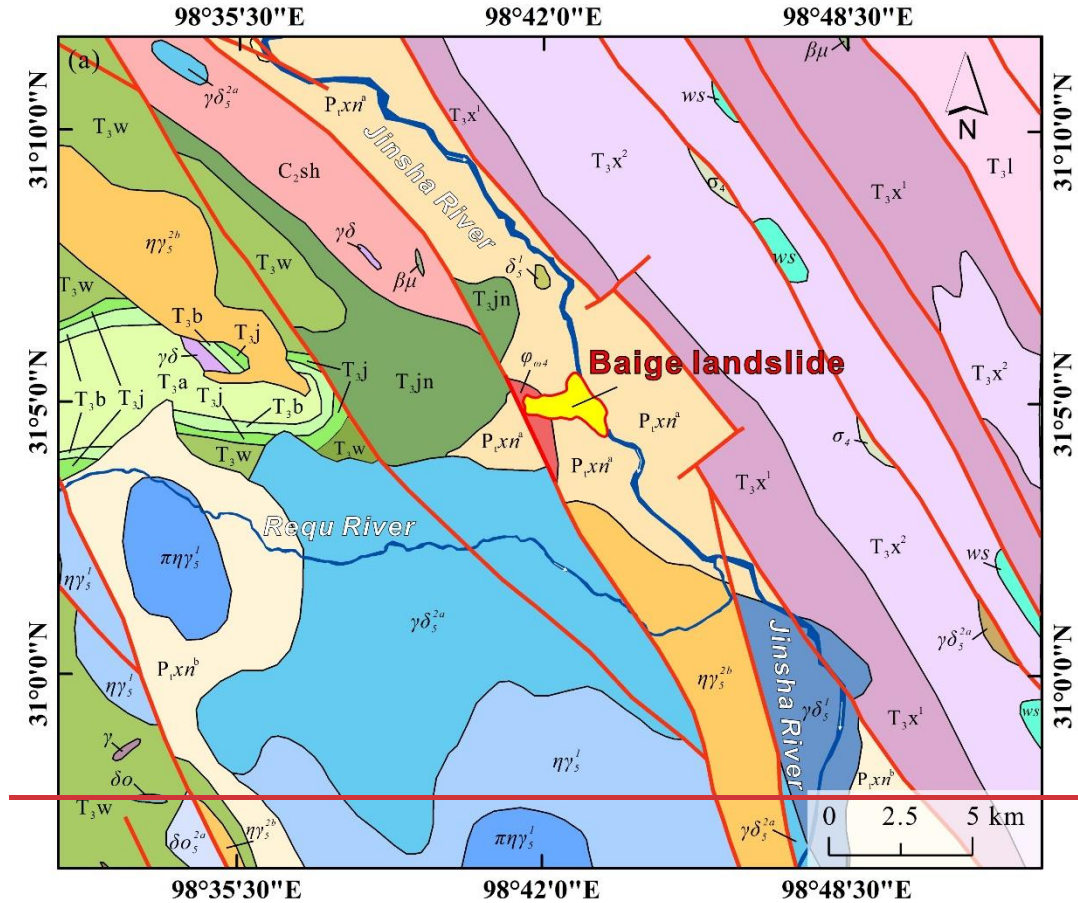


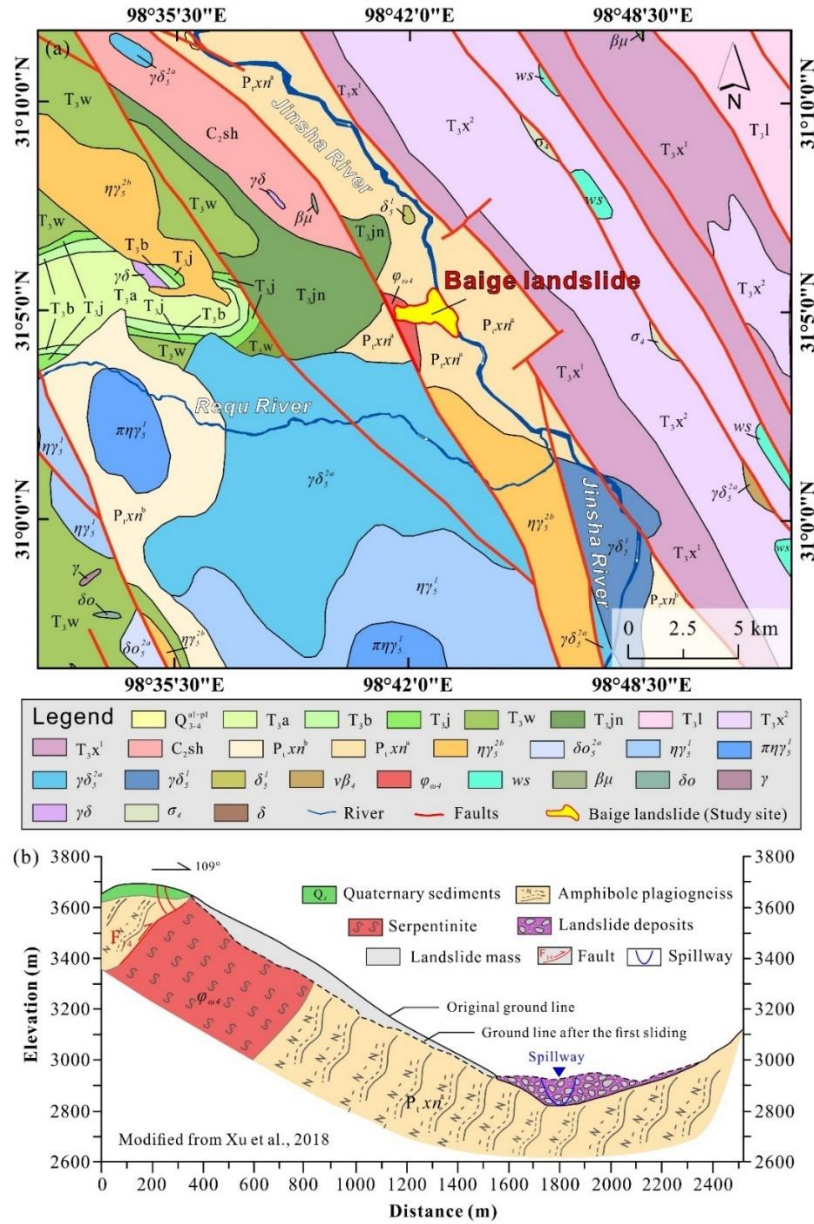
174



175

176 **Fig. 1.** Location of the study area. (a) DEMDigital Orthophoto Map (DOM) of Baige  
 177 landslide 2017; (b) DEMDOM of Baige landslide after the 2018 event; (c) Schematic cross-section  
 178 with remote sensing overlay showing key features of the Baige landslide (SA1 and SA2 is two  
 179 main accumulation zone, the debris of SA1 is main from shear area, while SA2 main from main  
 180 slip area and blocking area; SA3 is the left bank of the river, scoured by landslide debris; SA4 is a  
 181 small area of the right bank scoured by landslide debris; SA5 is the downstream left bank, which  
 182 is affected by the landslide body mix with the sandblasting water SA1 and SA2 is a secondary slip  
 183 zone formed by small fragments at the top of the dam body lose stability; SA3 is the left bank of  
 184 the river, scoured by landslide debris; SA4 is a small area of the right bank, scoured by landslide  
 185 debris; SA5 is the downstream left bank, which is affected by the landslide body mix with the  
 186 sandblasting water); (d) Location of the Baige landslide (red star) relative to seismic stations  
 187 (green triangles) used in the study. The remote sensing image map data of Fig 1.a. is from the ©  
 188 Google Earth 2017, and the data of Fig 1.b. and Fig 1.c. are from the authors' own UAVUnmanned  
 189 Aerial Vehicle (UAV) photography measurements.





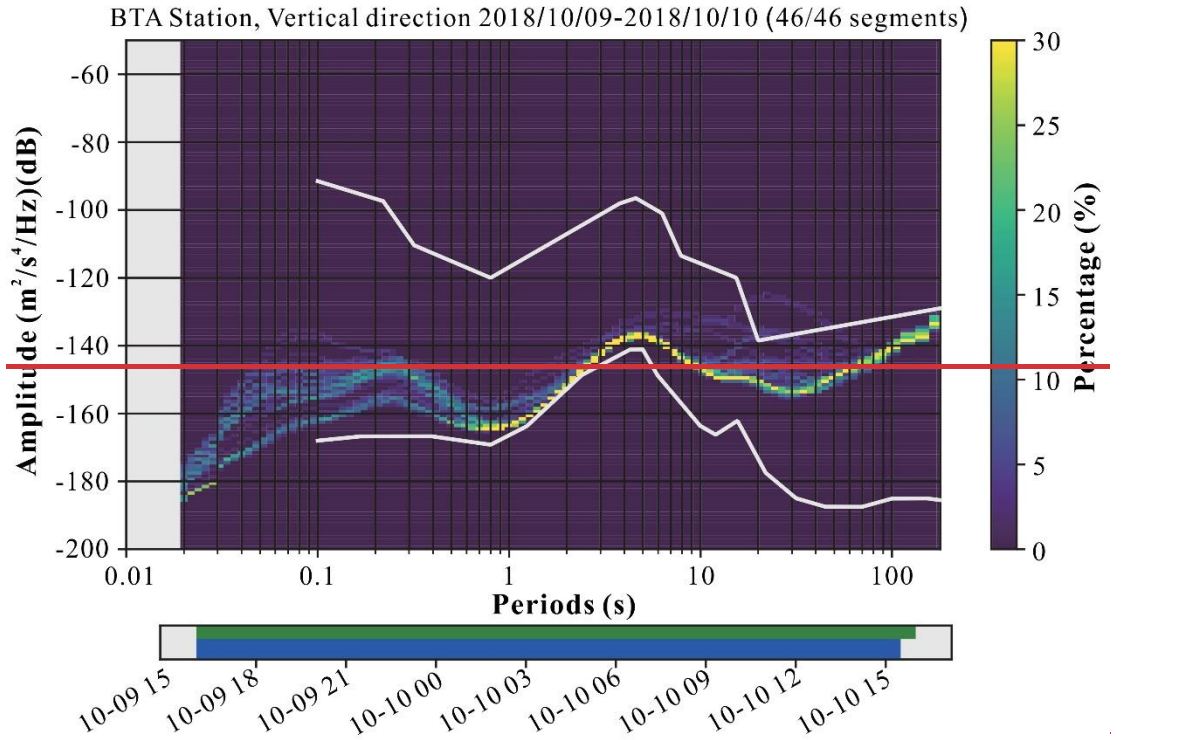
191

192 **Fig. 2.** Geology of the study area. (a) Geological map of the Baige landslide area ( $Q_{3-4}^{al-pl}$ ;  
 193 Quaternary Holocene Upper Pleistocene;  $T_{3a}$ ,  $T_{3b}$ ,  $T_{3j}$ ,  $T_{3w}$ ,  $T_{3jn}$ ,  $T_{3l}$ ,  $T_{3x^2}$ ,  $T_{3x^1}$ : Upper  
 194 Triassic;  $C_{2sh}$ : Upper Carboniferous;  $P_{xn^b}$ ,  $P_{xn^a}$ : Proterozoic;  $\eta\gamma_5^{2b}$ ,  $\delta\sigma_5^{2a}$ : Yanshan period;  
 195  $\eta\gamma_5^1$ ,  $\pi\eta\gamma_5^1$ ,  $\gamma\delta_5^{2a}$ ,  $\gamma\delta_5^1$ ,  $\delta_5^1$ : Indosinian;  $v\beta_4$ ,  $\varphi\omega_4$ ,  $\sigma_4$ : Variscan;  $ws$ : Detached block;  $\beta\mu$ :  
 196 Diabase-porphyrite;  $\delta o$ : Quartz diorite veins;  $\gamma$ : Granite veins;  $\gamma\delta$ : Granodiorite dikes;  $\delta$ : Diorite  
 197 veins.); (b) Cross-section of the landslide showing the geological profile. The geological map data  
 198 in Figure 2a is from Li et al., 2019a, and the cross-section in Figure 2b is modified from Xu et al.,  
 199 2018.

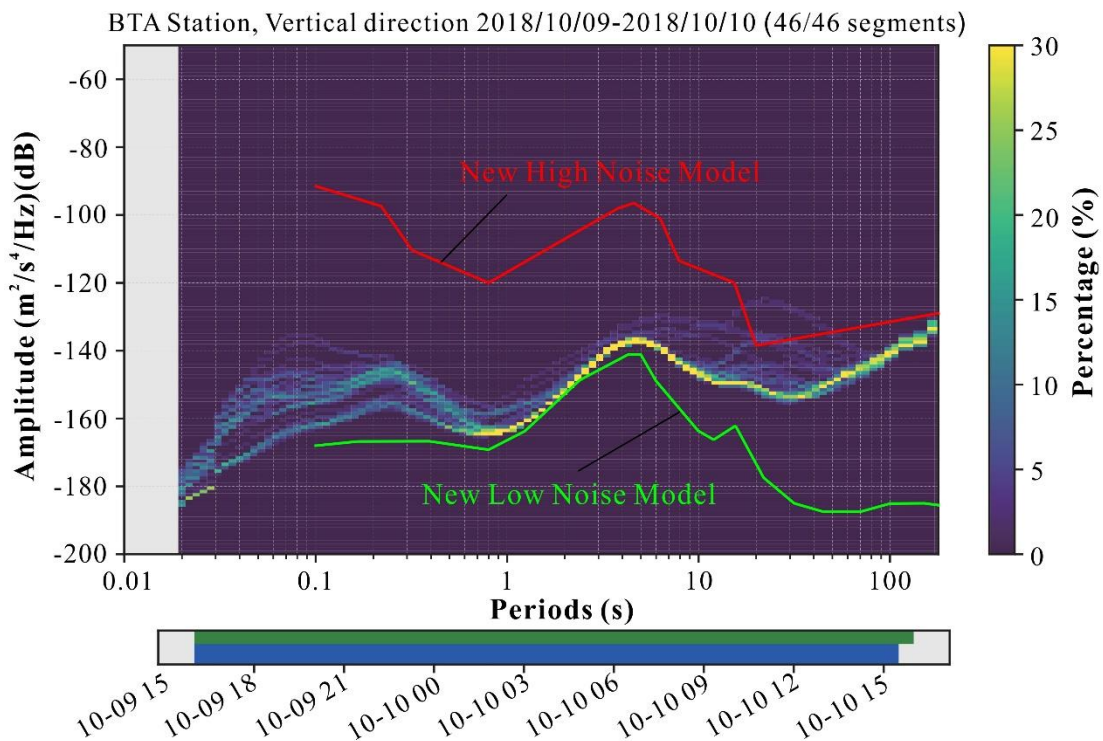
200  
201  
202  
203  
204  
205  
206  
207  
208  
209  
210  
211  
212  
213  
214  
215  
216  
217

We selected broadband seismic signals from seven seismic stations that are distributed around the landslide with adequate azimuth coverage (Fig. 1d) to carry out the analysis. Landslide force history inversion uses long-period seismic waveforms and thus requires that the ambient noise at periods of tens of seconds should be at a low level in the study area. We used the probabilistic power spectral density (PSD) technique (McNamara and Buland, 2004) to characterize the background seismic noise. As illustrated by the PSD of the vertical component for seismic station BTA (Fig. 3), the main seismic energy is distributed between the new high noise model (NHNM) and the new low noise model (NLNM) (Peterson, 1993), indicating that the study area has a relatively good seismic observation environment. Before carrying out the dynamic inversion, we will calculate the SNR for each seismic trace and use it to determine if the trace will be used in the inversion, about which a detailed description can be found in section 4.2 Dynamic inversion of landslide.

~~We selected broadband seismic signals from seven seismic stations that are distributed around the landslide with good azimuth coverage (Fig. 1d) to carry out the analysis. We used the probabilistic power spectral density (PSD) technique to obtain the background noise level of the selected seismic stations. As illustrated by the PSD of the vertical component for seismic station BTA (Fig. 3), the stations are characterized by low background noise ensuring good data quality.~~



218  
219



220

221 **Fig. 3.** Probabilistic power spectral density of the vertical component at seismic station BTA. Red  
 222 line in the PSD image is NHNM and green line is NLNM. White lines in the PSD image are NHNM

223 ~~(the upper one) and NLNM (the lower one).~~ Below the PSD image is a visualization of the data  
224 ~~basis for the calculation. The top row shows data fed into the calculation with green patches~~  
225 ~~representing available data. The bottom row in blue shows the single PSD measurements that go~~  
226 ~~into the histogram.~~

227

## 228 **3. Methodology**

### 229 **3.1 Seismic data analysis**

230 We used short-time Fourier transform (STFT) and PSD to quantitatively analyze the seismic  
231 signals for Baige landslide (Yan et al., 2020a, 2020b).~~We used short-time Fourier transform (STFT)~~  
232 ~~and PSD in the frequency domain to quantitatively analyze the time-frequency characteristics of~~  
233 ~~seismic signals for Baige landslide (Yan et al., 2020a, 2020b).~~ A ~~joint~~ time-frequency domain  
234 transform of the seismic signal using STFT allowed information on both the time and frequency  
235 domain distributions of the seismic signal to be obtained. The power of each unit of frequency for  
236 each frequency band component that corresponds to a specific moment was estimated based on  
237 the PSD of the seismic signal in the frequency domain.

### 238 **3.2 Landslide force history inversion**

239 Assuming the landslide source is represented as a series of time-varying forces acting on a  
240 static point, synthetic seismograms  $u_n(\mathbf{x}, t)$  at the seismic station located at  $\mathbf{x}$  can be computed  
241 by convolution of force  $f_i(\mathbf{x}_0, t_0)$  at  $\mathbf{x}_0$  with nine-component Green's functions  
242  $G_{ni}(\mathbf{x}, t; \mathbf{x}_0, t_0)$  ( Moretti et al., 2012; Allstadt, 2013; Ekström and Stark, 2013; Yamada et al.,  
243 2013; Hibert et al., 2014; Li et al., 2017; Gualtieri and Ekström, 2018),

$$244 \quad u_n(\mathbf{x}, t) = G_{ni}(\mathbf{x}, t; \mathbf{x}_0, t_0) * f_i(\mathbf{x}_0, t_0) \quad (1)$$

245 where  $*$  denotes convolution and bold type face indicates a vector. The Einstein summation  
 246 convention is assumed in the equation. The convolution can be rewritten as matrix product,

$$247 \quad \mathbf{u}_n = [\mathbf{G}_{n1} \quad \mathbf{G}_{n2} \quad \mathbf{G}_{n3}] \begin{bmatrix} \mathbf{f}_1 \\ \mathbf{f}_2 \\ \mathbf{f}_3 \end{bmatrix} \quad (2)$$

248 Suppose there are  $N$  seismic traces,

$$249 \quad \begin{bmatrix} \mathbf{u}_1 \\ \vdots \\ \mathbf{u}_N \end{bmatrix} = \begin{bmatrix} \mathbf{G}_{11} & \mathbf{G}_{12} & \mathbf{G}_{13} \\ \vdots & \vdots & \vdots \\ \mathbf{G}_{N1} & \mathbf{G}_{N2} & \mathbf{G}_{N3} \end{bmatrix} \begin{bmatrix} \mathbf{f}_1 \\ \mathbf{f}_2 \\ \mathbf{f}_3 \end{bmatrix} \quad (3)$$

250 Use  $\mathbf{u} = \begin{bmatrix} \mathbf{u}_1 \\ \vdots \\ \mathbf{u}_N \end{bmatrix}$ ,  $\mathbf{G} = \begin{bmatrix} \mathbf{G}_{11} & \mathbf{G}_{12} & \mathbf{G}_{13} \\ \vdots & \vdots & \vdots \\ \mathbf{G}_{N1} & \mathbf{G}_{N2} & \mathbf{G}_{N3} \end{bmatrix}$ , and  $\mathbf{f} = \begin{bmatrix} \mathbf{f}_1 \\ \mathbf{f}_2 \\ \mathbf{f}_3 \end{bmatrix}$ , we get the linear forward model

$$251 \quad \mathbf{u} = \mathbf{G}\mathbf{f} \quad (4)$$

252 We use  $\mathbf{u}_o$  to denote observed seismic records and define the 2-norm of the vector  
 253 difference between  $\mathbf{u}_o$  and  $\mathbf{u}$  as an objective function,

$$254 \quad \mathbf{o} = \|\mathbf{u} - \mathbf{u}_o\|_2 \quad (5)$$

255 An optimal solution of the forces can be obtained in a least-square sense,

$$256 \quad \mathbf{f} = (\mathbf{G}^T \mathbf{G})^{-1} \mathbf{G}^T \mathbf{u}_o \quad (6)$$

257 The landslide force history can be reconstructed by direct deconvolution of the observed  
 258 seismograms with Green's functions, which can be readily performed in both time and frequency  
 259 domains (Allstadt, 2013; Yamada et al., 2013; Li et al., 2017). We calculated Green's Function at  
 260 the landslide location for each seismic station, using a matrix propagation method (Wang, 1999)  
 261 and a 1-D layered velocity model from Crust1.0 (<https://igppweb.ucsd.edu/~gabi/crust1.html>).

262 Once the landslide force history  $\mathbf{f}$  was inverted, based on Newton's third law of motion, the  
 263 forces acting on the sliding mass could be obtained by multiplying the inverted force history by -  
 264 1 (Kanamori and Given, 1982; Yamada et al., 2013; Gualtieri and Ekström, 2018). And then the  
 265 forces acting on the sliding mass can be used to calculate its velocity and displacement

266 distributions for a given mass (Li et al., 2019c; Yu et al., 2020), or to estimate the sliding mass by  
267 minimizing discrepancies with independently derived sliding trajectories (Hibert et al., 2014),  
268 using the following equations,

$$269 \quad \mathbf{v} = - \int \frac{\mathbf{f}}{m} dt \quad (7)$$

$$270 \quad \mathbf{s} = - \iint \frac{\mathbf{f}}{m} dt \quad (8)$$

271  
272 ~~where \* denotes convolution and bold type face indicates a vector. The Einstein summation~~  
273 ~~convention is assumed in the equation. The landslide force history can be reconstructed by direct~~  
274 ~~deconvolution of the observed seismograms with Green's functions, which can be readily~~  
275 ~~performed in both time and frequency domains (Allstadt, 2013; Yamada et al., 2013; Li et al.,~~  
276 ~~2017). We calculated Green's Function at the landslide location for each seismic station, using a~~  
277 ~~matrix propagation method (Wang, 1999) and a 1-D layered velocity model from Crust1.0~~  
278 ~~(<https://igppweb.ucsd.edu/~gabi/crust1.html>).~~

279 ~~Seismic data were deconvolved with the instrument response to obtain displacement, a 4th-order~~  
280 ~~Butterworth bandpass filter in the frequency band of 0.006–0.2 Hz was then applied, and finally~~  
281 ~~the records were resampled to 0.2 s. Sixteen seismic traces with a signal to noise ratio (SNR)~~  
282 ~~larger than 10 dB were selected to carry out the inversion.~~

### 283 **3.3 Numerical modeling**

#### 284 **3.3.1 Discrete element method**

285 To quantitatively analyze the process of landslide initiation, movement, and accumulation for  
286 the "10.10" Baige event, we used MatDEM software, which is based on the matrix discrete element

287 method, to numerically simulate the landslide (Liu et al., 2017). In the discrete element method,  
 288 particle movement obeys Newton's second law, and particle velocity and displacement are  
 289 sequentially updated to simulate the dynamic process of the landslide. In MatDEM, the landslide  
 290 body is formed by the accumulation and cementation of particles endowed with specific  
 291 mechanical properties, and the contact and interaction of these particles are defined by the linear  
 292 elastic bonded model, as shown in Figure 4a. The normal force  $F_n$  and tangential force  $F_s$   
 293 between particles can be expressed by the following formula:

$$F_n = K_n X_n \quad (29)$$

$$F_s = K_s X_s \quad (310)$$

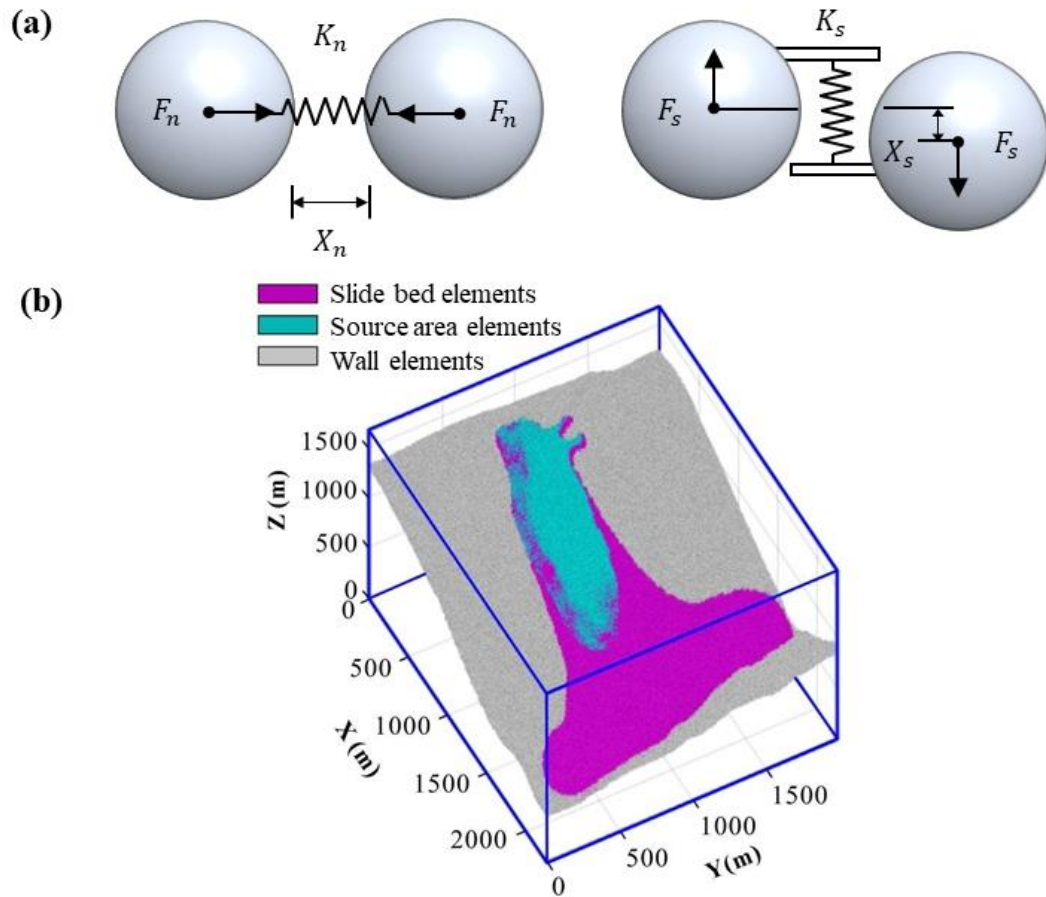
294 where,  $K_n$  is the normal stiffness;  $X_n$  is the normal relative displacement between two  
 295 particles at the contact point;  $K_s$  is the tangential stiffness; and  $X_s$  is the tangential  
 296 displacement.

297 In the normal direction, when the displacement between particles  $X_n$  exceeds the fracture  
 298 displacement  $X_b$  the connection between particles is broken and the tension is set as zero. In the  
 299 tangential direction, spring failure follows the Mohr-Coulomb criterion, and the tangential bond is  
 300 broken when tangential force exceeds maximum shear force  $F_{smax}$ , so that only sliding friction  
 301 ( $-\mu_p F_n$ ) exists between particles. The maximum normal force  $F_{nmax}$  and maximum tangential  
 302 force that the cementation between particles  $F_{smax}$  can withstand is:

$$F_{nmax} = K_n X_b \quad (411)$$

$$F_{smax} = F_{s0} - \mu_p F_n \quad (512)$$

303 where,  $F_{s0}$  is the shear resistance between particles and  $\mu_p$  is the friction coefficient  
 304 between particles.



305  
 306 **Fig. 4.** Schematics showing properties of landslide particles and discrete element model. (a) Linear  
 307 elastic bonded model; (b) Discrete element model of the Baige landslide (Fan et al., 2019a).  
 308

### 309 3.3.2 Discrete element model of Baige landslide

310 In MatDEM, the base of the landslide model is constructed of densely packed particles (20 m  
 311 thick) arranged according to the topography of the slope base. The coordinates of these particles  
 312 are fixed in the simulation (gray particles in Fig. 4b). The landslide area is constructed by cutting

313 particles accumulated in the cube model box using [cutting topography of](#) the pre- and post-  
314 landslide ~~topography~~. ~~We used terrain data from Ouyang et al. (2019), comprising a 10-m~~  
315 ~~resolution pre-landslide DEM from 2017, and a 5-m resolution post-slide DEM obtained through~~  
316 ~~UAV photogrammetry in 2018~~. Before starting the simulation, gravity is applied to particles in the  
317 sliding source area (blue particles in Fig. 4b) and sedimentary layer (20–80 m thick) (purple  
318 particles in Fig. 4b); breaking the connection between particles in the source area allows them to  
319 slide down under the action of gravity to simulate landslide initiation. We used a simulation [block](#)  
320 ~~area~~ of 2270×1980×1680 m, with 582,000 particles comprising 169,000 active cells for simulating  
321 landslide movement and 413,000 boundary [cells-elements](#) to fill the geometry (bottom) and limit  
322 the range of activity (side). Average cell size was 5 m and the real-world time 80 s.

323 [As shown in the flow chart of Fig. 5, we used the dynamic inverted from seismic signals and](#)  
324 [deposition characteristics as references for the DEM simulation. Initial macro parameter values,](#)  
325 [such as Young modulus, Poisson's ratio, were based on results of laboratory tests on Baige](#)  
326 [landslide materials from Zhou et al. \(2019\), the micro parameters, such as normal stiffness, shear](#)  
327 [stiffness, breaking displacement, initial shear resistance, of DEM input can be obtained by using](#)  
328 [the macro and micro conversion equations proposed by Liu et al. \(2013\) \(see Appendix 1 for](#)  
329 [details\). As elastic modulus and mechanical properties in laboratory tests are usually higher than](#)  
330 [those in large-scale rock masses in the field \(Darlington et al., 2011; Hencher et al., 2014; Hoek,](#)  
331 [2000\), Liu et al. \(2019\) used MatDEM to simulate Xinmo landslide, set Young's modulus and](#)  
332 [strength to about 40% of the test value, and obtained appropriate simulation results. Therefore, we](#)  
333 [used 40% of the test value in our simulation.](#)

334 The second step is to use the geometry of the deposits as a reference to adjust and obtain  
335 reasonable simulation result. For the discrete element method, the geometry of the deposits is  
336 affected by the bond strength between particles and the friction coefficient (An et al., 2020), which  
337 correspond to the fracture displacement, initial shear force, and friction coefficient between  
338 particles in MatDEM. Other parameters, such as normal stiffness and tangential stiffness, remain  
339 constant during the simulation. Accuracy of the final landslide accumulation was evaluated by the  
340 critical success index (CSI) proposed by Mergili et al. (2017), calculated as:

$$CSI = \frac{TP}{TP + FP + FN} \quad (13)$$

341 where, TP (true positive) is intersection area from both simulation and filed observation, FN  
342 (false negative) is the deposition area observed from field that simulation cannot covered, and FP  
343 (false positive) is the additional deposition area from simulation where no deposition is observed  
344 from site. CSI ranges between 0 and 1, and the higher the value, the more accurate the simulation;  
345 when CSI is 1, the simulated accumulation range coincides with the observed. An et al. (2021)  
346 conducted 25 simulations by changing the parameters such as static friction coefficient, thermal  
347 weakening friction coefficient and normal bond strength. The results showed that only 8 cases had  
348 CSI > 0.6 and the highest CSI was 0.83. In addition, among the 15 groups of results simulated by  
349 Mergili et al. (2017), the maximum CSI is 0.59. Therefore, in this study, the criterion is chosen as  
350 CSI > 0.6, it can be considered that the simulated accumulation characteristics are basically  
351 consistent with the actual situation.

352 The third step is to use the landslide motion velocity and displacement characteristics inverted  
353 by the seismic signal as a reference to back-calibrate parameters that affect the kinematic

354 characteristics of the landslide, such as friction and average damping coefficients. The final values  
355 of the parameters are shown in Table 1.

356 The accuracy of simulated and inversed landslide velocity and displacement was  
357 preliminarily evaluated by the relative errors of several key points  $\delta$ . Then, the square residue  $S^2$   
358 between the simulated value and the inversion value per second was calculated, and the difference  
359 between the two groups of data in the landslide process was analyzed in detail. Related error  $\delta$   
360 and square residue  $S^2$  were calculated as:

$$\delta_x = \frac{X_s - X_i}{X_i} \quad (14)$$

$$S^2 = (X_s - X_i)^2 \quad (15)$$

361 where,  $X_s$  is the simulated value and  $X_i$  the inversed value.  $X$  can be replaced by landslide  
362 duration  $T$ , peak velocity  $V_{max}$ , time when peak velocity achieved  $T_{V_{max}}$ , and peak displacement  
363  $D_{max}$ .

364 ~~We used the landslide initiation, dynamic, and deposition characteristics inverted from~~  
365 ~~seismic signals as a reference for the discrete element landslide motion simulation. Parameter~~  
366 ~~values were determined according to the accumulation state. For the discrete element method, the~~  
367 ~~range of landslide accumulation is affected by the bond strength between particles and the friction~~  
368 ~~coefficient (An et al., 2020), which correspond to the fracture displacement, initial shear force, and~~  
369 ~~friction coefficient between particles in MatDEM. Other parameters, such as normal stiffness and~~  
370 ~~tangential stiffness, remain constant during the simulation. Parameter values were based on results~~  
371 ~~of laboratory tests on Baige landslide materials in Zhou et al. (2019), using the macro and micro~~  
372 ~~conversion formula. This formula was an experience formula proposed by Liu et al. (2013), its~~

373 build a bridge from macro parameters to micro parameters. It used to obtain initial parameters of  
374 elements. While initial parameters still need to adjusted to obtain reasonable simulation result. As  
375 elastic modulus and mechanical properties in laboratory tests are usually higher than those in large-  
376 scale rock masses in the field, Liu et al. (2019) used MatDEM to simulate Xinmo landslide, set  
377 Young's modulus and strength to about 40% of the test value, and obtained appropriate simulation  
378 results. Therefore, refer to it, we used c. 40% of the test value in our simulation. The second step  
379 is to use the landslide motion velocity and displacement characteristics inverted by the ground  
380 motion signal as a reference to back determine parameters that affect the kinematic characteristics  
381 of the landslide, such as friction and average damping coefficients (a flow chart of the method is  
382 shown in Fig. 5, and the final values of the parameters are shown in Table 1). Accuracy of the final  
383 landslide accumulation was evaluated by the critical success index (CSI) proposed by Mergili et  
384 al. (2017), calculated as:

$$CSI = \frac{TP}{TP + FP + FN} \quad (6)$$

385 Where, TP (true positive) is where the simulated and observed accumulation areas intersect,  
386 FN (false negative) is where the simulated results show no accumulation, but the observed results  
387 do, and FP (false positive) is where the simulation result shows accumulation where none is  
388 observed. The sum of TP, FP, and FN is the union of the simulation and observation areas. CSI  
389 ranges between 0 and 1, and the higher the value, the more accurate the simulation; when CSI is  
390 1, the simulated accumulation range coincides with the observed. In this study, when CSI > 0.6, it  
391 can be considered that the simulated accumulation characteristics are basically consistent with the  
392 actual situation. This is because it is not easy to obtain the simulation results of CSI > 0.6 in

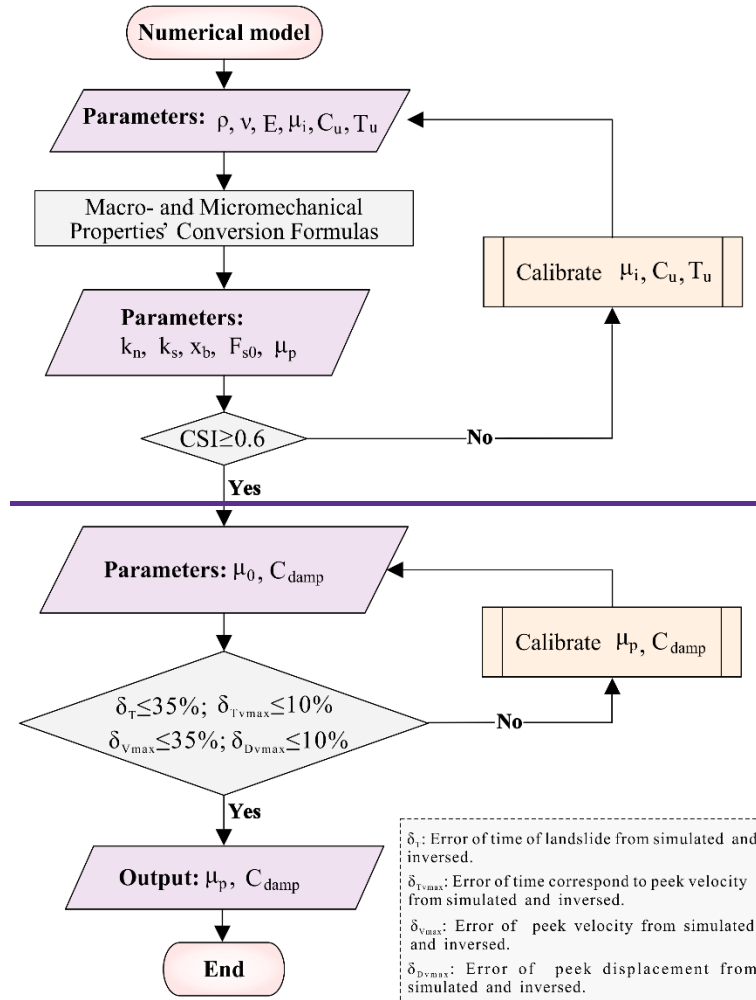
393 previous studies. For example, An et al. (2021) conducted 25 simulations by changing the  
394 parameters such as static friction coefficient, thermal weakening friction coefficient and normal  
395 bond strength. The results showed that only 8 had CSI > 0.6 and the highest CSI was 0.83. Among  
396 the 15 groups of results simulated by Mergili et al. (2017), the maximum CSI is 0.59.

397  
398 The accuracy of simulated and inversed landslide velocity and displacement was  
399 preliminarily evaluated by the relative errors of several key points  $\delta$ . Then, the variance  $S^2$  between  
400 the simulated value and the inversion value per second was calculated, and the difference between  
401 the two groups of data in the landslide process was analyzed in detail. Related error  $\delta$  and  
402 variance  $S^2$  were calculated as:

$$\delta_x = \frac{X_s - X_t}{X_t} \quad (7)$$

$$S^2 = (X_s - X_t)^2 \quad (8)$$

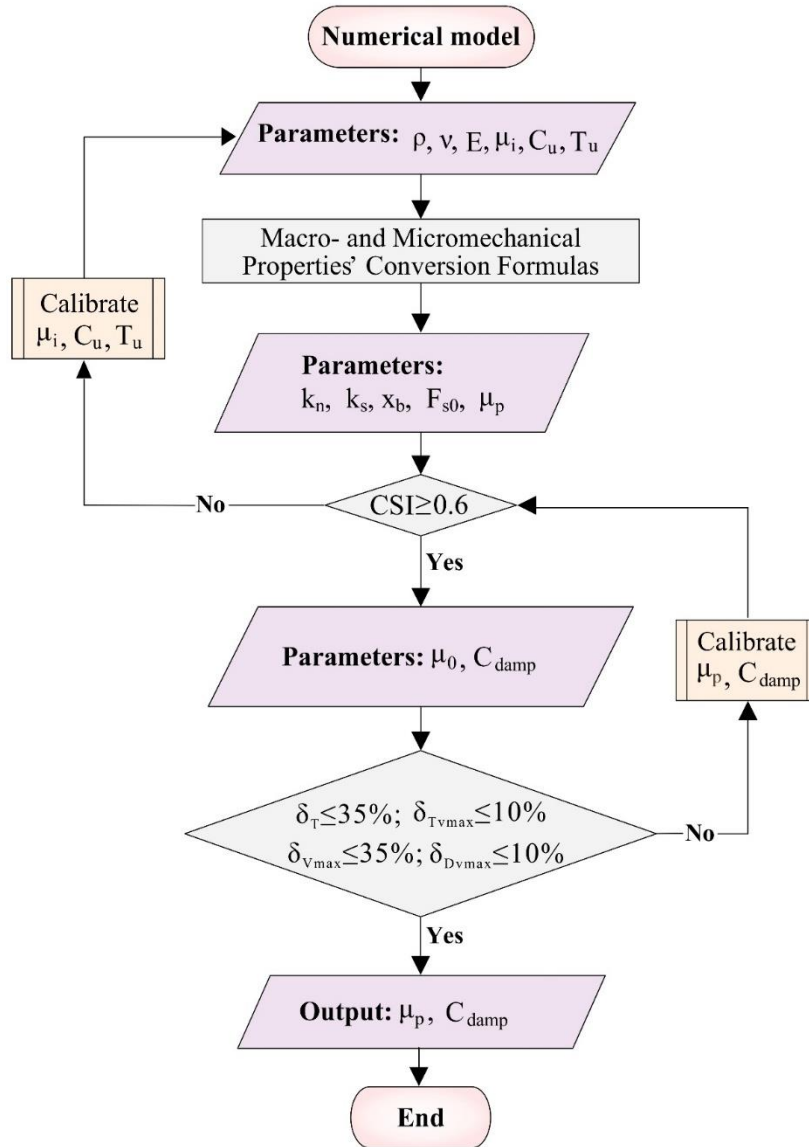
403 Where,  $X_s$  is the simulated value and  $X_t$  the inversed value.  $X$  can be replaced by landslide  
404 duration  $T$ , peak velocity  $V_{max}$ , peak velocity corresponding to time  $T_{vmax}$ , and peak displacement  
405  $D_{max}$ .



406

407

408



409

410 **Fig. 5.** Flowchart of the method of discrete element parameter adjustment based on seismic signal  
 411 inversion.

412

413 **Table 1.** Macro- and micromechanical parameters of Baige landslide material used in the  
 414 discrete element model.

<u>Parameter</u>	<u>Value</u>	<u>Reference</u>
<u>Young modulus <math>E</math></u>	<u>20 GPa</u>	<u>Laboratory test (Zhou et al. 2019)</u>
<u>Poisson's ratio <math>\nu</math></u>	<u>0.2</u>	<u>Laboratory test (Zhou et al. 2019)</u>
<u>Uniaxial compressive strength <math>C_u</math></u>	<u>30 MPa</u>	<u>Laboratory test &amp; Calibrated</u>
<u>Uniaxial tensile strength <math>T_u</math></u>	<u>3 MPa</u>	<u>Laboratory test &amp; Calibrated</u>

<u>Internal friction coefficient <math>\mu_i</math></u>	<u>0.46</u>	<u>Laboratory test &amp; Calibrated</u>
<u>Density <math>\rho</math></u>	<u>2400 kg/m<sup>3</sup></u>	<u>Zhang et al. (2019)</u>
<u>Normal stiffness <math>k_n</math></u>	<u>486 GN/m</u>	<u>Calculated (Liu et al., 2013)</u>
<u>Shear stiffness <math>k_s</math></u>	<u>270 GN/m</u>	<u>Calculated (Liu et al., 2013)</u>
<u>Breaking displacement <math>x_b</math></u>	<u>1.3 mm</u>	<u>Calculated (Liu et al., 2013)</u>
<u>Initial shear resistance <math>F_{s0}</math></u>	<u>3.28 GN</u>	<u>Calculated (Liu et al., 2013)</u>
<u>Intergranular friction coefficient <math>\mu_p</math></u>	<u>0.0897</u>	<u>Calculated &amp; Calibrated</u>
<u>Average damping coefficient <math>C_{damp}</math></u>	<u><math>1.06 \times 10^5</math></u>	<u>Calibrated</u>

415

<u>Parameter</u>	<u>Value</u>
<u>Young modulus <math>E</math></u>	<u>20 Gpa</u>
<u>Poisson's ratio <math>\nu</math></u>	<u>0.2</u>
<u>Uniaxial compressive strength <math>C_u</math></u>	<u>30 Mpa</u>
<u>Uniaxial tensile strength <math>T_u</math></u>	<u>3 Mpa</u>
<u>Internal friction coefficient <math>\mu_i</math></u>	<u>0.46</u>
<u>Density <math>\rho</math></u>	<u>2400 kg/m<sup>3</sup></u>
<u>Normal stiffness <math>k_n</math></u>	<u>486 GN/m</u>
<u>Shear stiffness <math>k_s</math></u>	<u>270GN/m</u>
<u>Breaking displacement <math>x_b</math></u>	<u>1.3mm</u>
<u>Initial shear resistance <math>F_{s0}</math></u>	<u>3.28GN</u>
<u>Intergranular friction coefficient <math>\mu_p</math></u>	<u>0.0897</u>
<u>Average damping coefficient <math>C_{damp}</math></u>	<u><math>1.06 \times 10^5</math></u>

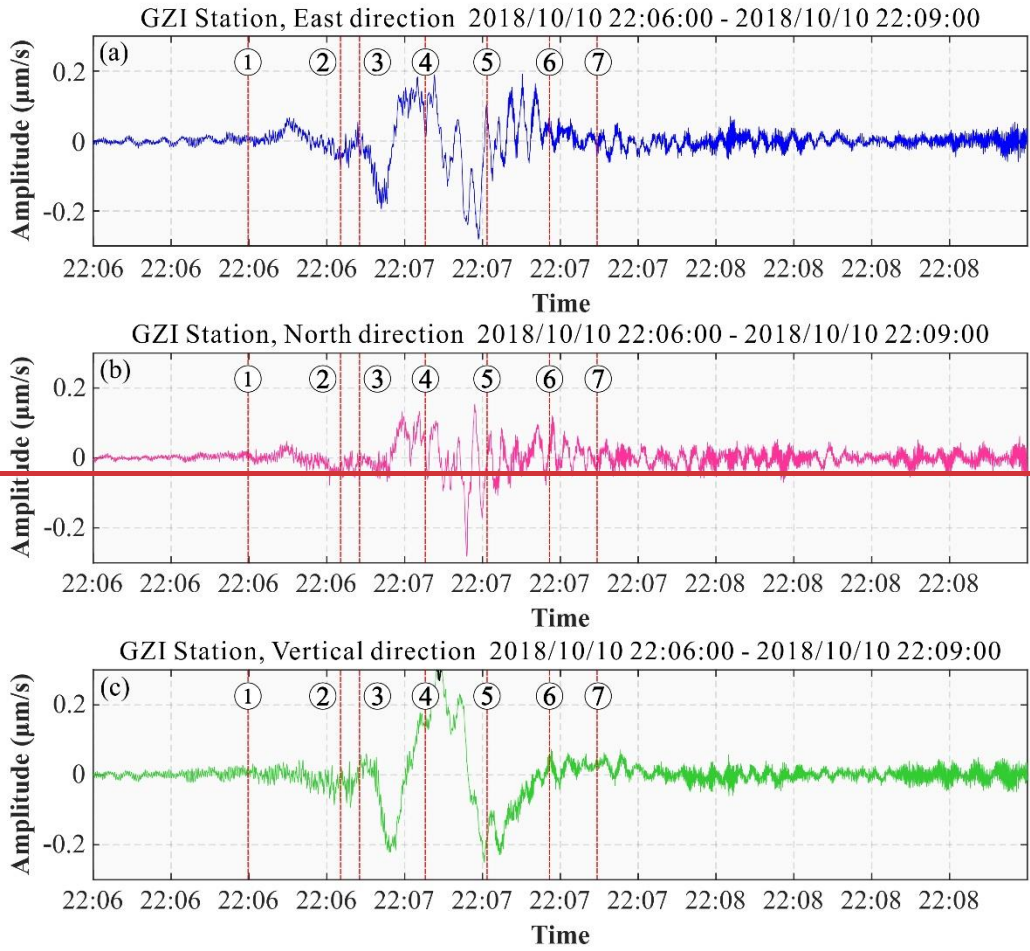
416

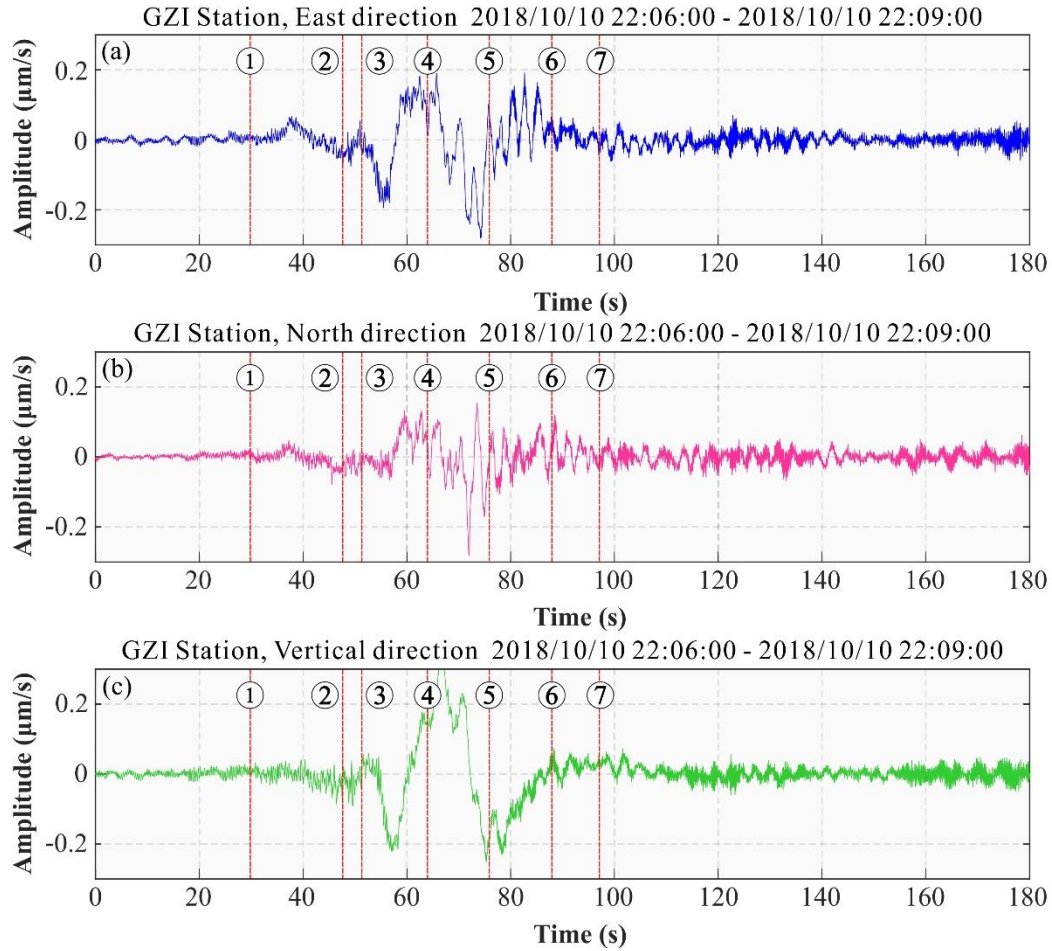
## 417 **4. Results and analysis**

### 418 **4.1 Seismic signal analysis**

419 The time-domain velocity curve of the seismic signal generated by the “10.10” Baige  
420 landslide is shown in Figure 6. The SNR of the vertical (V) and east (E) components is relative  
421 higher, compared with north (N) component, roughly reflecting the main slide direction of

422 ~~landslide is E and N. Post-event geological survey showed sliding was mainly in south-east-to-~~  
423 ~~south, approximately eastwards. The SNR of the vertical (V) and north (N) components is high,~~  
424 ~~and that of the east (E) component is low, reflecting the primary downslope direction of landslide~~  
425 ~~movement; post-event geological survey showed sliding was mainly in a south-east to south~~  
426 ~~direction.~~ The ~~main~~ driving force of the landslide is gravity, and the ~~surface on which the mass~~  
427 ~~slides~~ ~~landslide surface~~ is inclined at about 35°, so ~~velocity~~ ~~acceleration~~ ~~velocity~~ changes in the  
428 longitudinal direction are relatively large, and the SNR of the V component of the landslide signal  
429 appears high. ~~During the deposition stage, the main horizontal movement direction of landslide~~  
430 ~~body change from east-west to north-south, and from north-south limited to east-west limited. The~~  
431 ~~morphology of the landslide path~~ ~~channel~~ means that the landslide stage has a large east-west  
432 ~~component and a small north-south component, and in the deposition~~ ~~accumulation~~ stage, it  
433 ~~reverses. This feature is consistent with the high SNR of the N component at the end of~~ ~~of the~~  
434 ~~landslide signal and low SNR of the E component.~~ ~~During the deposition~~ ~~accumulation~~ stage, the  
435 ~~main landslide body moved in an easterly direction, with limited north-south sliding. The~~  
436 ~~morphology of the landslide channel means that the landslide body has a large east-west~~  
437 ~~component and a small north-south component. This feature is consistent with the high SNR of~~  
438 ~~the N component of the landslide signal and low SNR of the E component.~~





440

441 **Fig. 6.** Time-domain velocity/acceleration signal (E-N-V direction) of the seismic generated by the  
 442 Baige landslide at GZI seismic station, showing a relative high signal-to-noise ratio visually but  
 443 different respectively (①~⑦ refer to the characteristic stage of the Baige landslide) Time-domain  
 444 velocity curve of the seismic signal generated by the Baige landslide at seismic station GZI (see  
 445 Figure 1 for location) showing signal-to-noise ratio of the low-frequency components (E-N-V  
 446 direction).

447

448 The sliding distance of the landslide was c. 600 m longitudinally and c. 100 m laterally, while  
 449 the receiving stations are over 100 km away; as the sliding scale is relatively small relative to the  
 450 propagation distance, we treated it as a point source. The velocity curve recorded at a seismic  
 451 station is the velocity of the crustal vibration below the landslide area propagating to the station,  
 452 and this is roughly determined by velocity and mass of the landslide body. Therefore,

453 characteristics of the landslide downward movement can be obtained by analyzing the velocity  
454 curve recorded at seismic stations. The seismic signal from station GZI (Fig. 6) provides an  
455 example to show the general seismic characteristics of the “10.10” Baige landslide. The time-  
456 domain ~~velocity~~~~acceleration~~~~velocity~~ curve recorded at GZI determines the start time of the  
457 landslide as 22:06 on October 10, 2018 (all times are UTC+8), with a duration of about 76 s  
458 between 22:06:39 to 22:07:51. Five points of ~~velocity~~~~acceleration~~~~velocity~~ change are apparent  
459 during the landslide process (Fig. 6, Table 2), dividing the event into three phases of  
460 ~~acceleration~~~~velocity~~ and three of deceleration.

461 Due to seismic wave propagation, the start time determined by the original seismic signal at  
462 the station is slightly later than the true time; ~~what’s more, the signal is mixed by longitudinal wave~~  
463 ~~that stack with transverse wave, which makes the ending time picked by seismic signal much latter~~  
464 ~~than the actual time. All these make the duration of the landslide derived from the original seismic~~  
465 ~~signal would be lagged and longer, compared to the real time~~~~what’s more, the signal is a mixed~~  
466 ~~signal that longitudinal wave stack with transverse wave, which makes the ending time picked by~~  
467 ~~seismic signal. All these make the critical time of the landslide derived from the original seismic~~  
468 ~~signal would be lagged and longer duration time, compared to the reality.~~, ~~and the signal may also~~  
469 ~~be affected by superimposition of vertical and horizontal waves, which makes the end time lag.~~  
470 ~~So, the critical moments of the landslide derived from the original seismic signal would be lagged,~~  
471 ~~and the duration too long.~~—A more accurate landslide ~~duration~~time can be determined by ~~landslide~~  
472 ~~force history inversion~~~~inversion~~ as it eliminates the propagation effect. ~~The analysis of the velocity~~  
473 ~~curve recorded at seismic stations~~The analysis here ~~helps to help~~ understand the overall

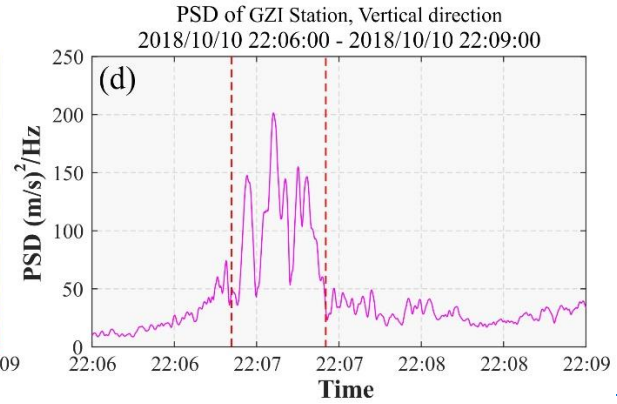
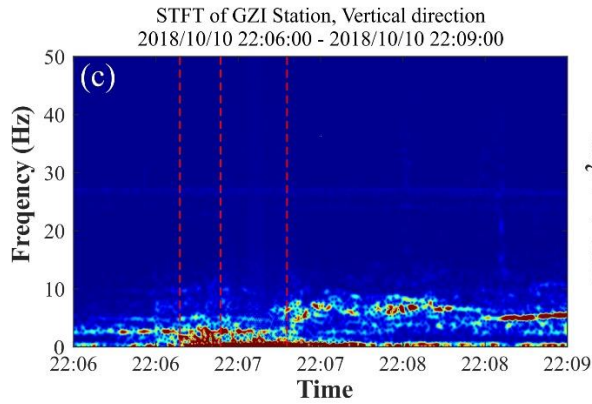
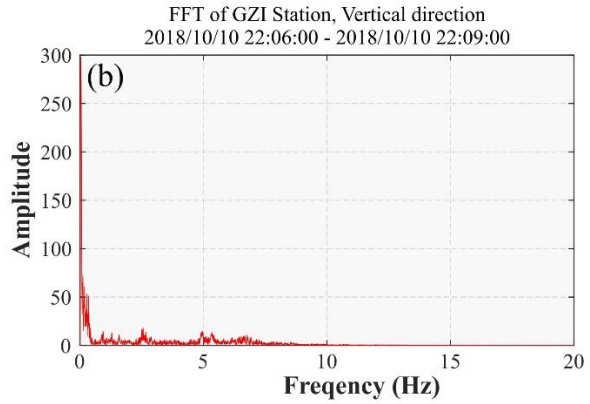
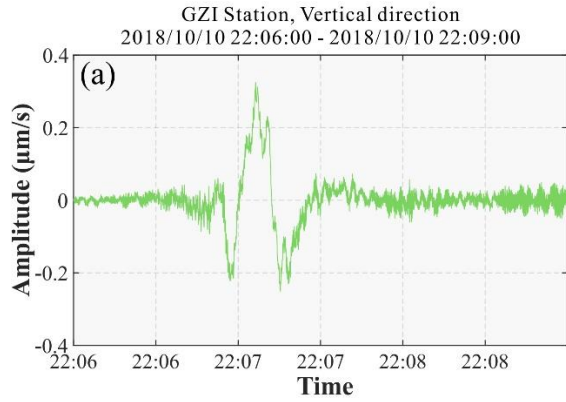
474 characteristics of the landslide and help verify the rationality of the subsequent Green's function  
 475 stress inversion results.

476 **Table 2.** The beginning characteristic stage of the Baige landslide river blocking event picked  
 477 by seismic signal recorded at GZI station~~Characteristic time of the seismic signal of the Baige~~  
 478 ~~landslide river blocking event (recorded at GZI station).~~

Landslide stage						
Start Time	deceleration	acceleration	deceleration	acceleration	deceleration	End Time
22:06:39	22:06:51	22:06:54	22:07:01	22:07:12	22:07:27	22:07:51

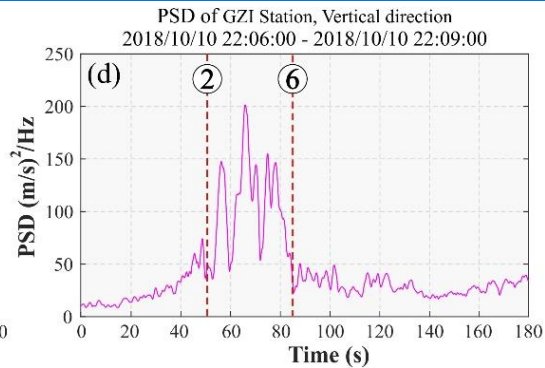
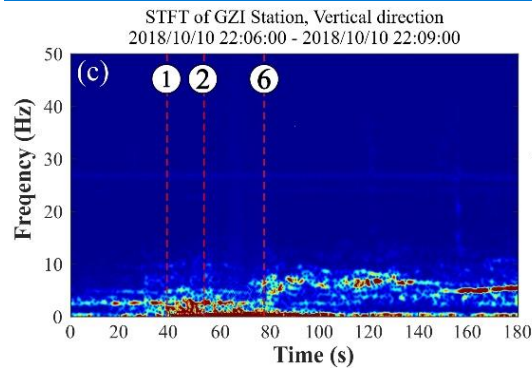
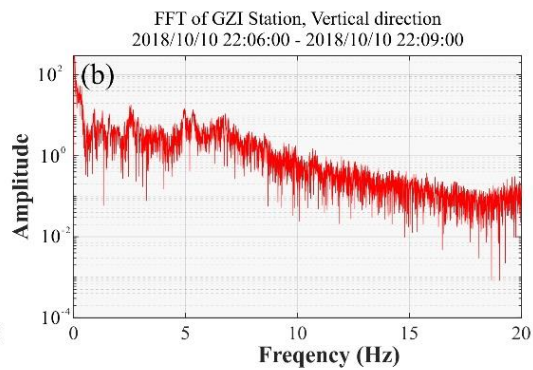
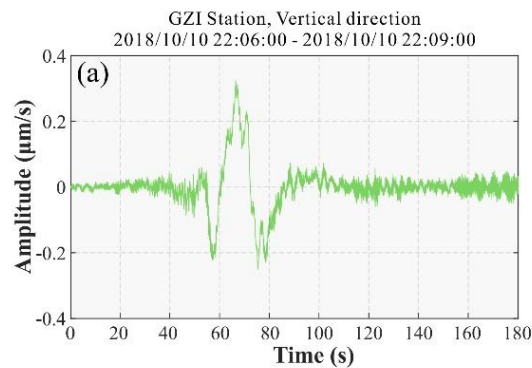
479

480 The start and end time of sliding is demarcated on the time spectrum of the seismic curve  
 481 (Fig. 7); strong energy clusters appear around 22:06:39, the intensity begins to decrease at 22:06:54  
 482 (UTC+8), and the frequency band narrows and the energy disappears at 22:07:27 (UTC+8). The  
 483 time spectrum shows the landslide was concentrated between 22:06:40–22:07:01. The frequency  
 484 is concentrated in the 0–1 Hz range, and the low-frequency component has a high SNR (0–0.2 Hz),  
 485 which is conducive to dynamic inversion.

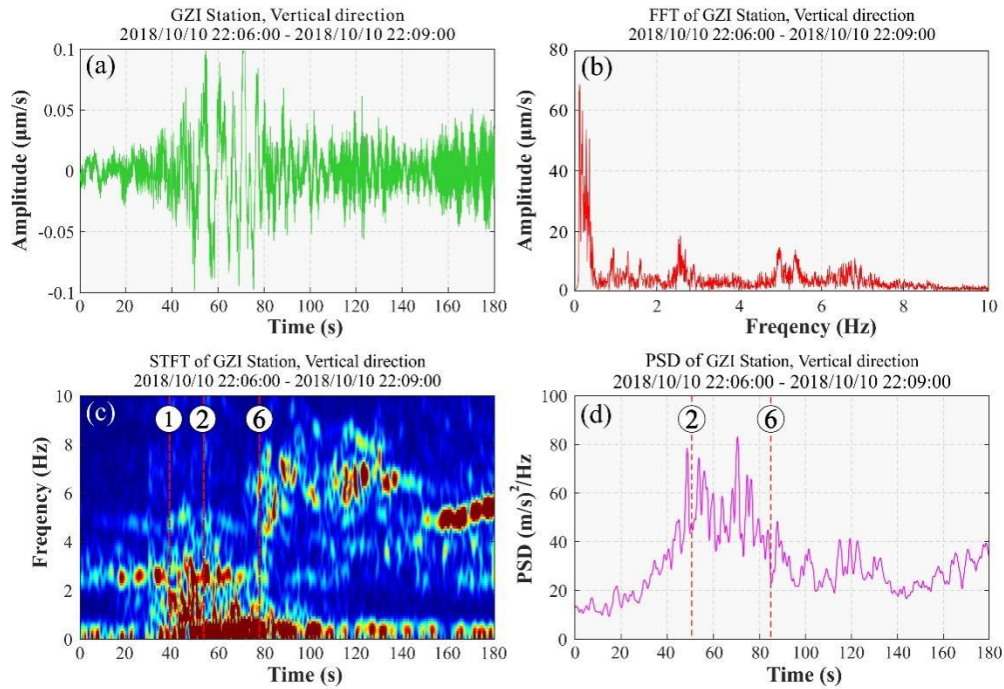


486

487



488



489  
 490 **Fig. 7.** Seismic signals of the Baige landslide as recorded at seismic station GZI. (a) Vertical  
 491 seismic signal; (b) Frequency spectrum; (c) Time-frequency spectrum; and (d) Power spectral  
 492 density (PSD) curve. Fig. 7. Seismic signals of the Baige landslide as recorded at seismic station  
 493 GZI. (a) Vertical seismic signal; (b) Frequency spectrum; (c) Time-frequency spectrum and the  
 494 key times picked frequency from it, that is, start time, 1st acceleration and 3rd deceleration, from  
 495 left to right respectively; and (d) Power spectral density (PSD) curve and the key times picked  
 496 from it, that is 1st acceleration and 3rd deceleration.

497  
 498 In Figure 7d, the PSD curve is divided into three stages in the longitudinal direction, with the  
 499 first and third stages corresponding to slow sliding and the second stage to fast sliding. Comparing  
 500 with the time domain stages (as in Table 2), the first PSD stage corresponds to the first  
 501 acceleration and deceleration, the second stage corresponds to the second deceleration,  
 502 acceleration and third deceleration, and the third stage corresponds to the third deceleration. The  
 503 PSD curve shows a marked increase in the second stage, indicating rapid downslope sliding, with  
 504 multiple large fluctuations indicating rapid changes in landslide movement that are characteristic  
 505 of the sliding stage.

506 According to Yan et al (2021), the frequency of landslide hazard seismic signals is usually  
507 low (0~5 Hz), and the morphology in the time-frequency domain and time domain presents single-  
508 peak or double-peak characteristics; while the frequency of flood or high-density flow seismic  
509 signals is usually high (5~50 Hz), and its morphology in the time-frequency domain and time  
510 domain is mostly flat. and the morphology in the time-frequency domain and time domain mostly  
511 presents the characteristics of flat. Combined with this landslide seismic signal has relatively low  
512 frequency (0~1 Hz) and the single-peak feature in time and time-frequency characteristics,  
513 apparently different from the spectrum (main frequency :15~30 Hz) of the outburst flood signal  
514 triggered by the second landslide on October 12, 2018 (Xu et al., 2018An et al, 2021). So, we think  
515 there was no flood discharge during the landslide process.The low frequency of the landslide  
516 seismic signal (0 1 Hz) and the single-peak waveform and time-frequency characteristics suggest  
517 there was no flood discharge during the landslide process. Typically, water flow generates a higher  
518 frequency (ranging between 0 50 Hz, but mainly 10 40 Hz) (Yan et al., 2017), and the duration  
519 and other characteristics are different; also, there is a clear difference from the outburst flood signal  
520 on October 12, 2018.

## 521 **4.2 Dynamic inversion of landslide**

522 The inverted force histories are shown in Fig. 8. The good fit of the synthetic and recorded  
523 Seismic data were processed using the following procedure before carrying out the landslide force  
524 history inversion. Firstly, they were deconvolved with the instrument response to obtain  
525 displacement; then a 4th-order Butterworth bandpass filter in the frequency band of 0.006–0.2 Hz  
526 was then applied; and finally, the records were resampled at a sampling rate of 5 Hz. The processed

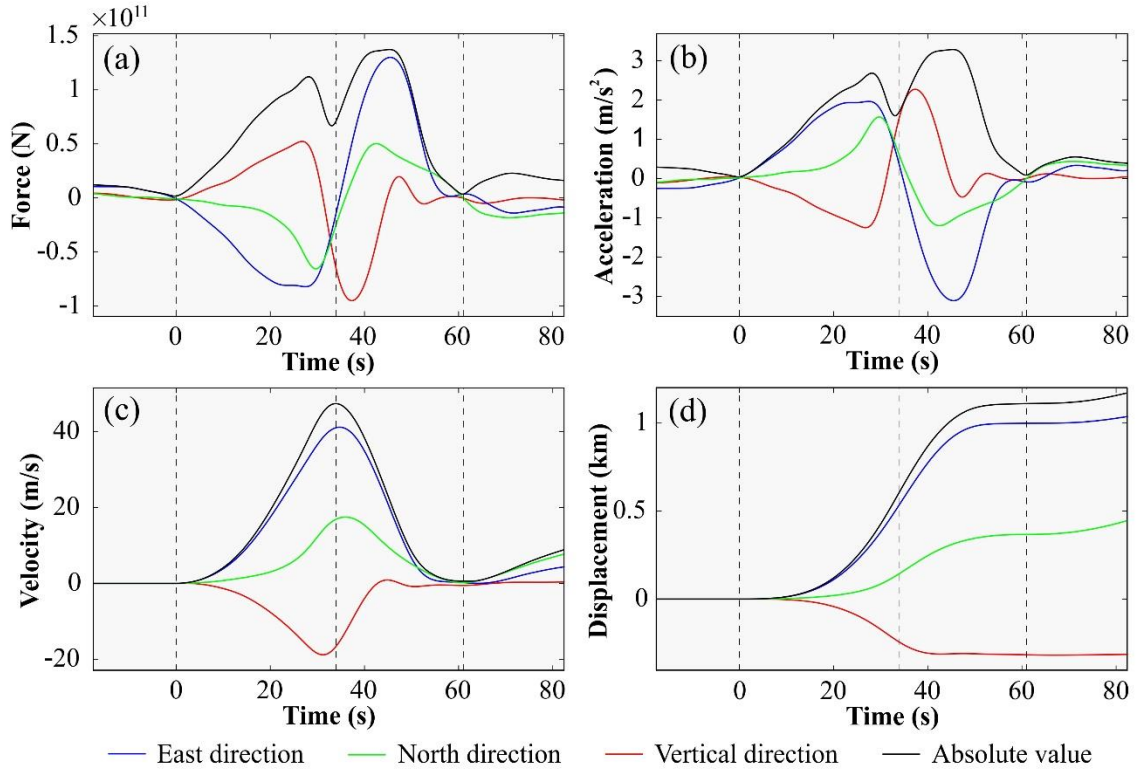
527 seismic records have a high signal-to-noise ratio (SNR) as shown in Table 43. Sixteen seismic  
 528 traces with an SNR larger than 10 dB were selected to carry out the inversion.

529 **Table 3.1** SNR of seismic signals used in the inversion and CC and VR of the inversion results

<u>Seismic Station</u>		<u>SNR</u>	<u>CC</u>	<u>VR</u>
<u>BTA</u>	<u>Z</u>	<u>19.19</u>	<u>0.96</u>	<u>0.90</u>
	<u>E</u>	<u>4.28</u>	<u>0.56</u>	<u>0.28</u>
	<u>N</u>	<u>8.45</u>	<u>0.60</u>	<u>0.34</u>
<u>GZI</u>	<u>Z</u>	<u>29.63</u>	<u>0.99</u>	<u>0.99</u>
	<u>E</u>	<u>20.39</u>	<u>0.99</u>	<u>0.98</u>
	<u>N</u>	<u>15.29</u>	<u>0.97</u>	<u>0.94</u>
<u>LTA</u>	<u>Z</u>	<u>24.67</u>	<u>0.99</u>	<u>0.98</u>
	<u>E</u>	<u>7.92</u>	<u>0.86</u>	<u>0.71</u>
	<u>N</u>	<u>15.12</u>	<u>0.97</u>	<u>0.94</u>
<u>DFU</u>	<u>Z</u>	<u>23.60</u>	<u>0.99</u>	<u>0.99</u>
	<u>E</u>	<u>17.58</u>	<u>0.99</u>	<u>0.98</u>
	<u>N</u>	<u>5.92</u>	<u>0.54</u>	<u>0.28</u>
<u>YJI</u>	<u>Z</u>	<u>22.58</u>	<u>0.98</u>	<u>0.97</u>
	<u>E</u>	<u>11.64</u>	<u>0.93</u>	<u>0.85</u>
	<u>N</u>	<u>16.75</u>	<u>0.95</u>	<u>0.90</u>
<u>YUS</u>	<u>Z</u>	<u>18.05</u>	<u>0.94</u>	<u>0.89</u>
	<u>E</u>	<u>19.39</u>	<u>0.98</u>	<u>0.97</u>
	<u>N</u>	<u>18.01</u>	<u>0.98</u>	<u>0.96</u>
<u>BAM</u>	<u>Z</u>	<u>21.48</u>	<u>0.99</u>	<u>0.98</u>
	<u>E</u>	<u>5.86</u>	<u>0.74</u>	<u>0.53</u>
	<u>N</u>	<u>10.91</u>	<u>0.94</u>	<u>0.88</u>

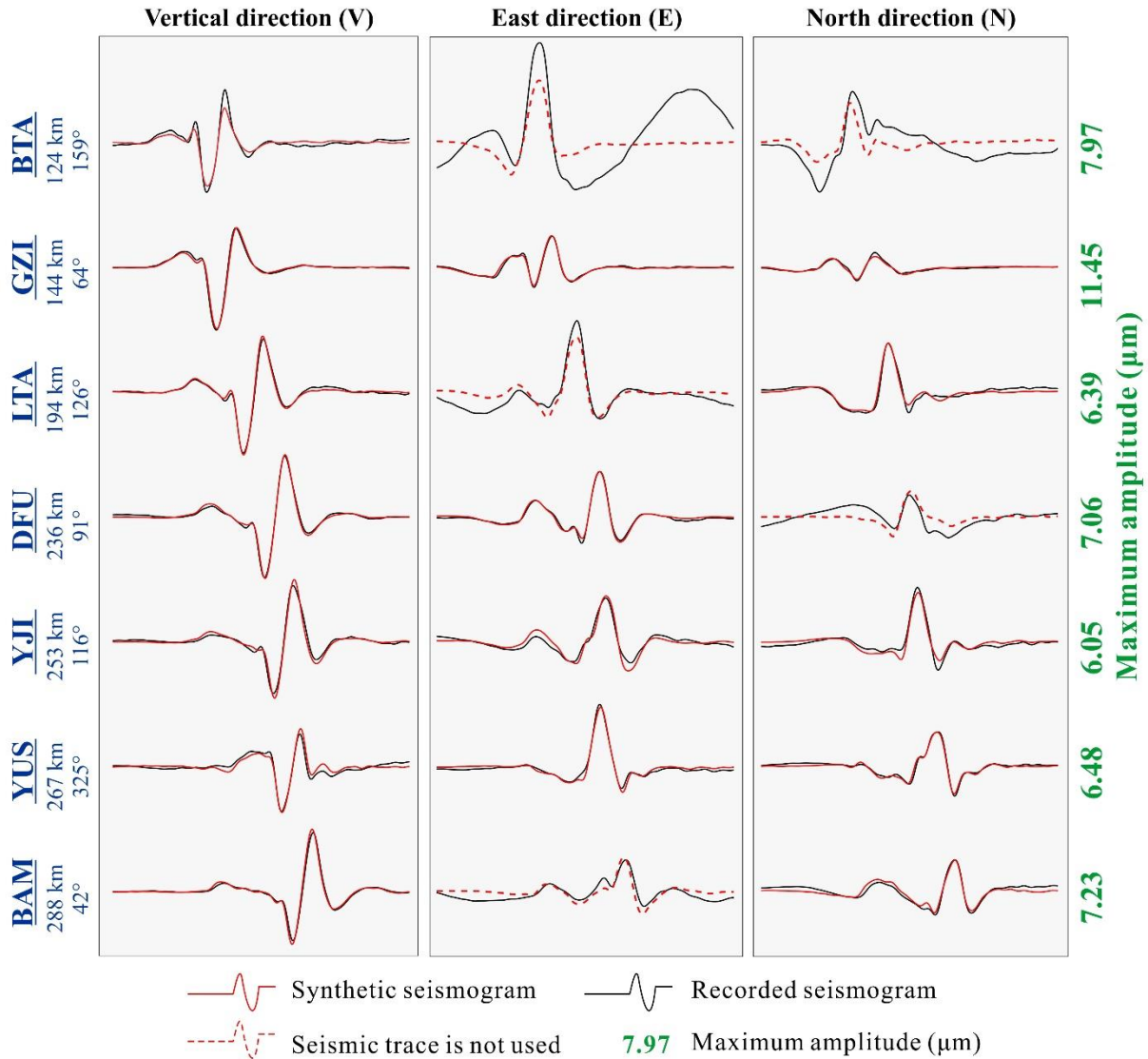
530 The inverted force histories are shown in Fig. 8. The good fit of the synthetic and recorded  
 531 seismic waveforms in Fig. 9 and the high cross-correlation (CC) and variance reduction (VR)  
 532 between synthetic and recorded seismograms provided in Table 3 Table 4 indicate the high quality  
 533 of the inversion results. The inverted forces show landslide initiation at 14:05:37.6, with ~61 s  
 534 duration of the main motion. seismic waveforms in Fig. 9 indicates the high quality of the inversion  
 535 results. The inverted forces show landslide initiation at 14:05:37.6, with ~61 s duration of the main  
 536 motion. Using the empirical relationships of Chao et al. (2016) and Ekström and Stark (2013), the

537 maximum force of  $1.37 \times 10^{11}$  N gives an estimated sliding mass of  $5.5 \times 10^{10}$  kg and  $7.4 \times 10^{10}$  kg,  
 538 respectively.



539 — East direction — North direction — Vertical direction — Absolute value

540 **Fig. 8.** Dynamic inversion used to obtain Baige landslide characteristics. **(a)** Inverted force time  
 541 history; **(b)** Estimated acceleration distribution over time; **(c)** Reconstructed velocity distribution  
 542 over time from the inverted landslide force time history; **(d)** Reconstructed displacement  
 543 distribution over time from the inverted landslide force time history. Corresponding absolute  
 544 values are shown as dashed-black lines. Dashed vertical black lines marked the landslide start and  
 545 end times (the first and third ones) and the time that the sliding mass reached the maximum speed  
 546 (the middle one). Corresponding absolute values are shown as dashed black lines.



547

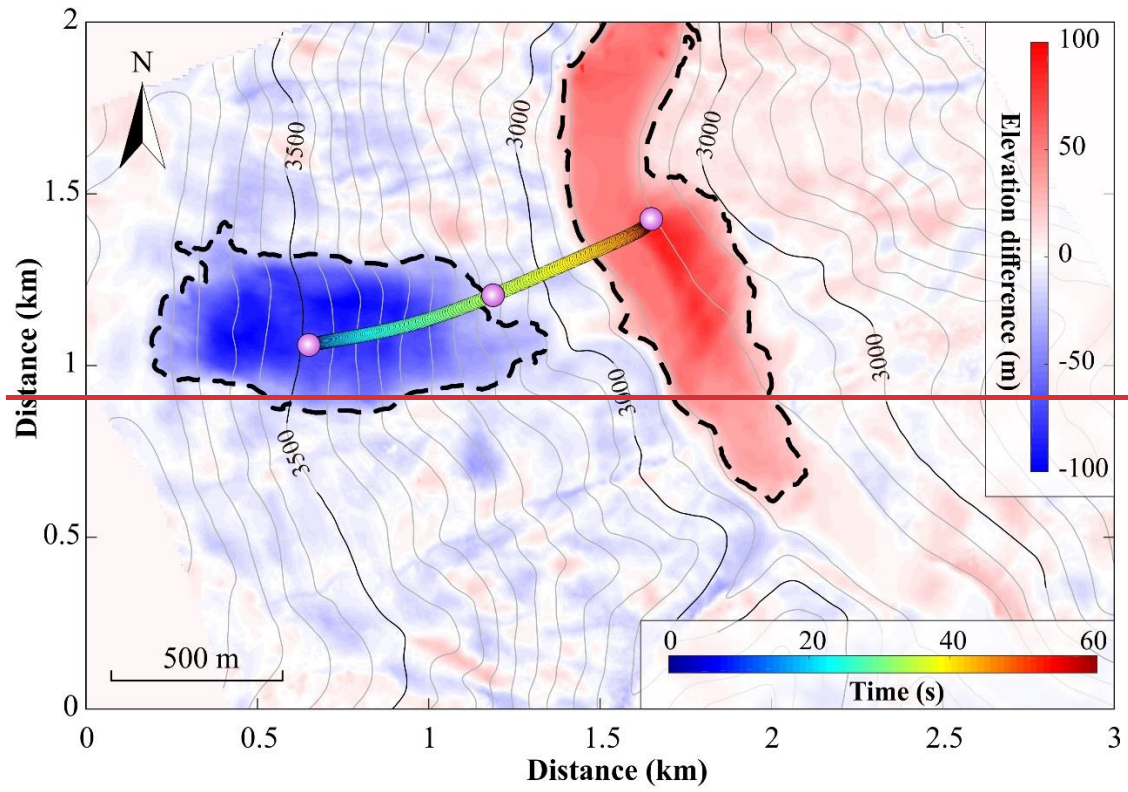
548 **Fig. 9.** Seismograms of the Baige landslide. Synthetic (red lines) and recorded (black lines)  
 549 seismograms are compared. Red dotted lines indicate that the seismic trace was not used in the  
 550 inversion because their SNR is smaller than 10 dB. Station name, distance from study site (km)  
 551 and azimuth (degree) are given to the left of each trace (see Fig. 1d for locations), and the  
 552 maximum amplitude of the three components is given in  $\mu\text{m}$  to the right.

553

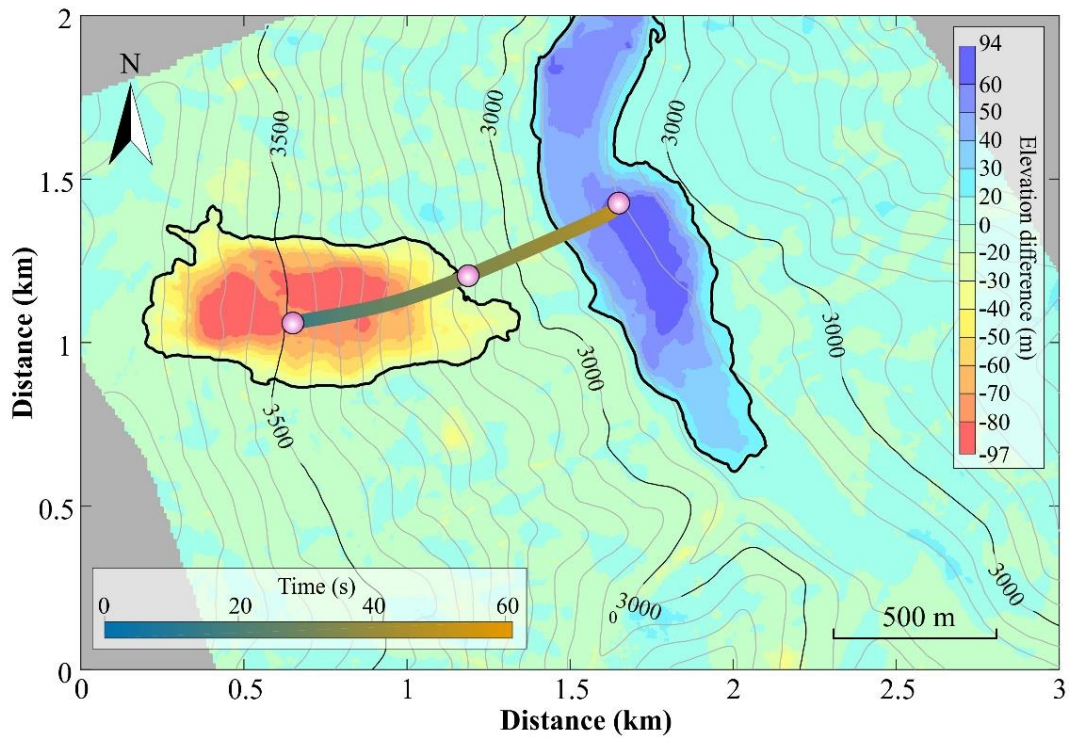
554 By comparing the DEMs before and after the event, we determined the mass centers of the  
 555 source area and the depositional area and subsequently derived the displacement of the center of  
 556 the sliding mass; then, by minimizing the predicted and actual displacements, we adopted the

557 ~~second approach and~~ estimated the sliding mass as ~~c.~~  $4.2 \times 10^{10}$  kg. The recovered sliding ~~horizontal~~  
558 ~~and vertical~~ trajectories ~~ies~~ both fit well with the observations, shown in Fig. 10. We used the  
559 ~~estimated sliding mass to determine the acceleration and,~~ velocity, ~~and displacement~~ distributions  
560 ~~over time (Figs. 8b to 8d).~~

561 ~~Based on Newton's third law of motion, the forces acting on the sliding mass are obtained by~~  
562 ~~multiplying the inverted force history by -1 (Kanamori and Given, 1982; Yamada et al., 2013;~~  
563 ~~Gualtieri and Ekström, 2018). We can then use this force to calculate velocity and displacement~~  
564 ~~distributions of the sliding material for a given mass (Li et al., 2019c; Yu et al., 2020), or to~~  
565 ~~estimate the sliding mass by minimizing discrepancies with observed sliding trajectories derived~~  
566 ~~from satellite images (Hibert et al., 2014). We adopted the second approach and estimated the~~  
567 ~~sliding mass as c.  $4.2 \times 10^{10}$  kg. The recovered horizontal and vertical trajectories both fit well with~~  
568 ~~the observations, shown in Fig. 10. We used the estimated sliding mass to determine the~~  
569 ~~acceleration, velocity, and displacement distributions over time (Figs. 8b to 8d).~~



570



571

572 **Fig. 10.** Reconstructed horizontal trajectory of the Baige landslide from the seismic dynamic  
 573 inversion. The base map is the elevation difference derived from DEMs and the reconstructed  
 574 trajectory is shown by the colored dots and connecting timeline.

575

576 The inversion results show two stages of landslide movement, 34 s of acceleration followed  
577 by 27 s of deceleration, which are separated by the vertical dashed black lines in Fig. 8. The sliding  
578 mass reached a maximum velocity of 47.4 m/s at the end of the acceleration stage and then rapidly  
579 decelerated (Fig. 8c). At c. 50 s, the vertical component shows reverse force and velocity,  
580 indicating this was when the main sliding mass traveled over the Jinsha River. The force of the E  
581 and V components increases in a nearly linear manner in the first 26 s, but then decreases rapidly,  
582 ~~indicating that the sliding mass was subject to relatively high frictional force after 26 s~~. The  
583 reconstructed horizontal trajectory of the landslide (Fig. 10) indicates that the front of the sliding  
584 mass ran up the opposite valley wall after it crossed the Jinsha River, ~~which would explain the~~  
585 ~~relatively high frictional force~~.

### 586 **4.3 Numerical modeling results**

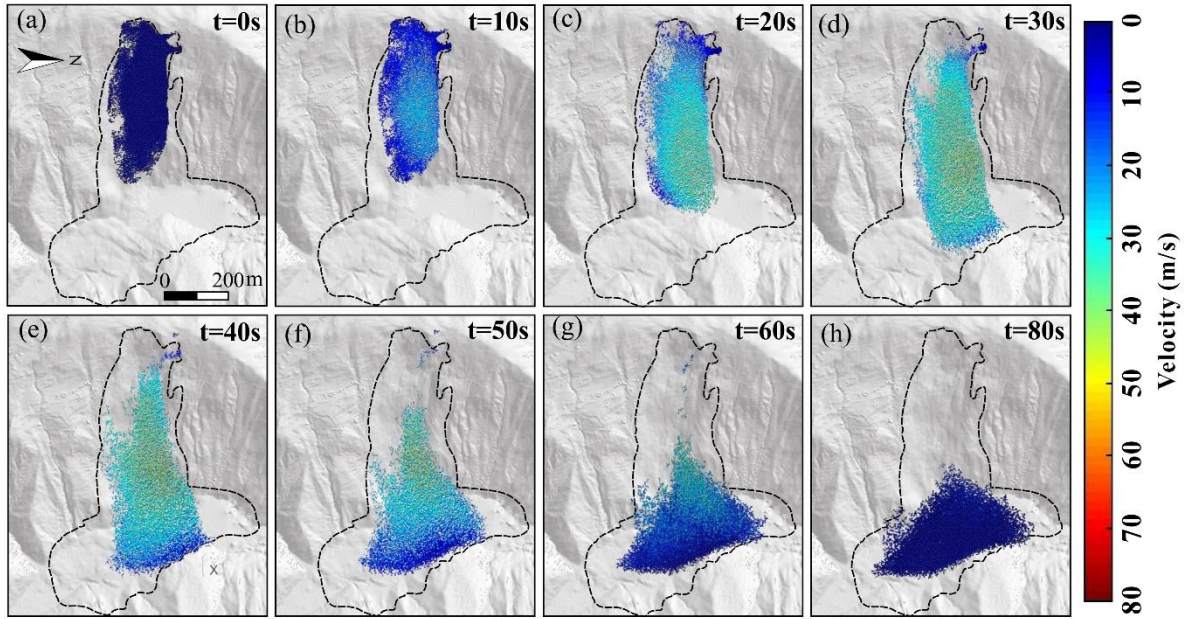
587 According to the results of numerical simulation ~~The-the~~ movement process of the “10.10”  
588 Baige landslide can be divided into three stages: (1) sliding (0–20 s); (2) acceleration when  
589 entering the river (20–40 s); and (3) diffusion and accumulation (40–80 s). The velocity  
590 distribution through each stage of the simulated landslide is shown in Figure 11.

591 At the start of the simulation, the connection between particles inside and outside the sliding  
592 source area was broken simultaneously to initiate the landslide, which then rapidly fell with a  
593 constant (gravitational) acceleration. Due to the small particle friction coefficient (0.0897),  
594 simulated average velocity and average displacement growth rate are both higher than that  
595 determined in the inversion until 18 s, but their variation trends are similar, ~~after which they match~~.

596 From the [square residue variance](#) results, there is little difference between the simulated and  
597 inverted landslide velocity and displacement at this stage, as shown in Fig. 12.

598 In the second stage, the landslide body is moving downwards at a constant acceleration in the  
599 simulation, but the inversion shows increased acceleration; so, simulated average velocity and  
600 displacement appear to be substantially lower than the inversion. However, the time to reach peak  
601 velocity is similar for the simulation (32.8 s) and inversion (32 s). For both velocity and  
602 displacement, [square residue variance](#) between the inversion and simulation reaches a maximum  
603 in this stage, with  $R^2$ - $S^2$  of  $2.19 \times 10^2$  and  $2.88 \times 10^4$ . At 40 s, the particles at the front edge of the  
604 landslide are stationary due to the obstacle provided by the valley wall/mountain slope on the  
605 opposite bank of Jinsha River.

606 In the third stage, from 40 s, particles in the middle and rear of the landslide body continue  
607 to move downwards, spreading and accumulating along the river, with a constant deceleration.  
608 After 60 s, the simulated average displacement reaches 1020 m and levels off thereafter, which  
609 corresponds well with the inversion. Most particles in the landslide body have accumulated and  
610 are stationary at this stage, but a few particles on the trailing edge are still moving. By 80 s, the  
611 average velocity tends to 0, showing that landslide movement has ended. [The square residue](#)  
612 [variance of velocity residuals](#) ~~The velocity variance~~ has a secondary peak around 50 s, while the  
613 displacement [square residue variance](#) decreases gradually. Overall, the simulated accumulation  
614 area is relatively small compared with that derived from DEM differencing, although the location  
615 of maximum thickness corresponds well (Fig. 13b). The CSI is calculated as 0.65, which suggests  
616 the simulation is moderately good.

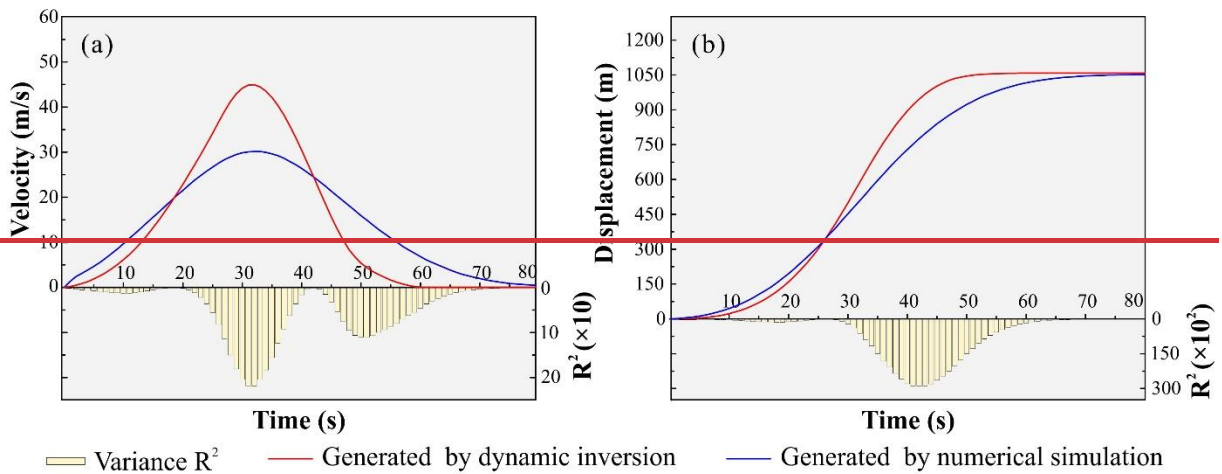
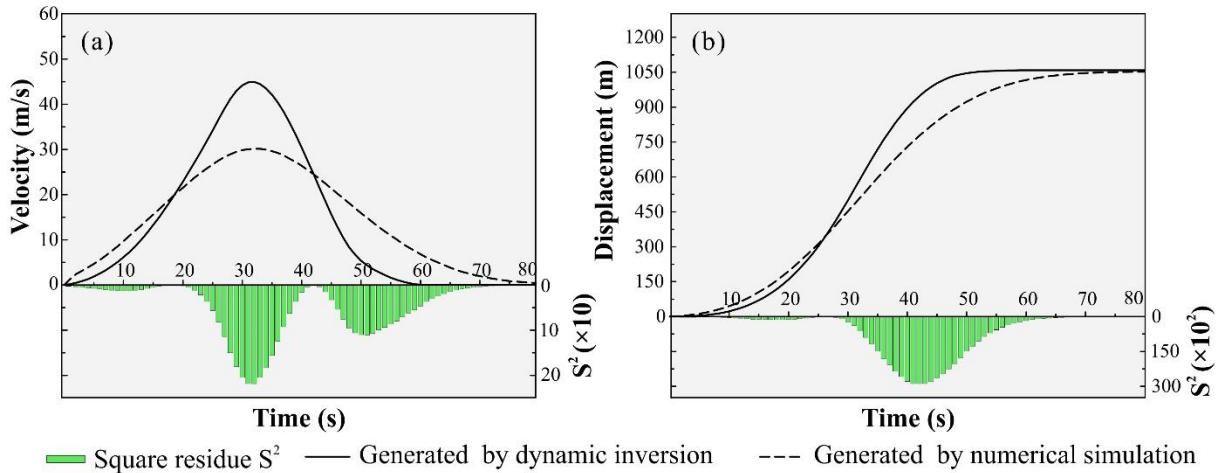


617

618 **Fig. 11.** Simulated landslide velocity distribution calculated in MatDEM. **(a)**  $t = 0$  s; **(b)**  $t = 10$  s;  
 619 **(c)**  $t = 20$  s; **(d)**  $t = 30$  s; **(e)**  $t = 40$  s; **(f)**  $t = 50$  s; **(g)**  $t = 60$  s; **(h)**  $t = 80$  s. The digital terrain model  
 620 (DTM) data of Fig 11. are from the authors' own UAV photography measurements.

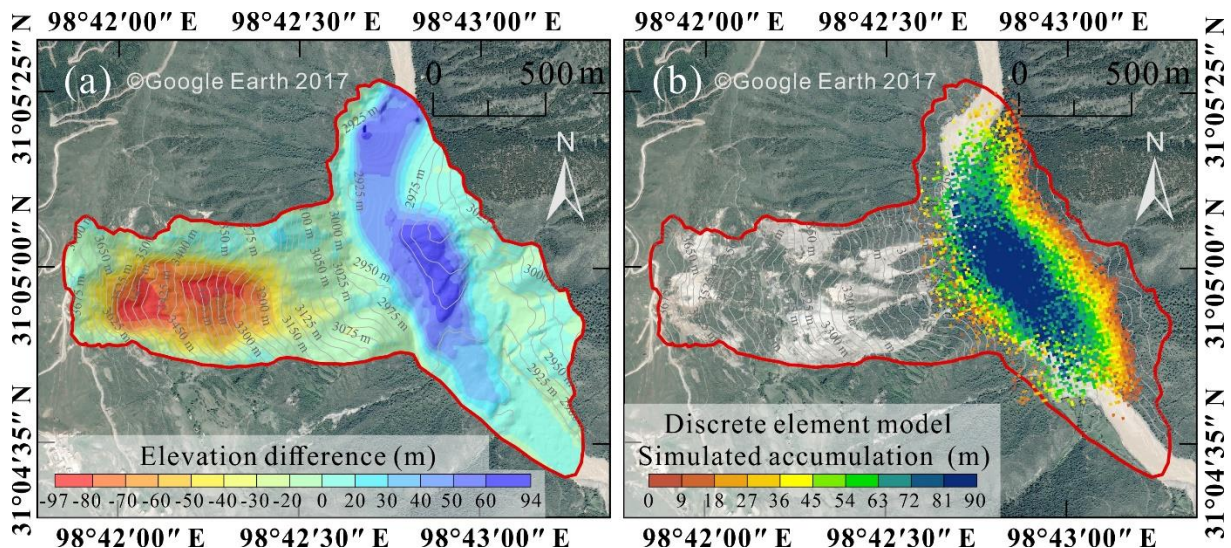
621

622



625

626 **Fig. 12.** Comparison of landslide characteristics simulated using discrete element model with  
 627 inversion results. **(a)** Average velocity; **(b)** Average displacement.



630 **Fig. 13.** Comparison of elevation change associated with the Baige landslide. **(a)** Estimated from  
631 pre- and post-failure topography; **(b)** Calculated using the discrete element model. The remote  
632 sensing image map data of Fig 13.a. and b. are from the © Google Earth 2017.

633

## 634 **5. Discussion**

### 635 **5.1 Field observation and dynamic inversion**

636 ~~Our estimates of the sliding mass from inversion data, based on the empirical relationships~~  
637 ~~Using the empirical relationships of Chao et al. (2016) and Ekström and Stark (2013), the~~  
638 ~~maximum inverted force of  $1.37 \times 10^{11}$  N gives an estimated sliding mass of  $5.5 \times 10^{10}$  kg and~~  
639  ~~$7.4 \times 10^{10}$  kg, respectively, which are about 1.32 and 1.77 times of our estimation of about  $4.2 \times 10^{10}$~~   
640 ~~kg from landslide force inversion. We further use a density of  $2.4 \times 10^3$  kg/ m<sup>3</sup> (Zhang et al., 2019)~~  
641 ~~to estimate the volumes corresponding to these masses. The results are  $1.75 \times 10^7$ ,  $2.29 \times 10^7$ , and~~  
642  ~~$3.08 \times 10^7$  m<sup>3</sup>, accounting for 89%, 117%, and 157% of that derived from DEM differences. All~~  
643 ~~estimated volumes are consistent with the DEM-derived volume in general, only that the estimates~~  
644 ~~from empirical relationships are slightly larger. This is not surprising as we used a different~~  
645 ~~frequency band in our inversion (0.006–0.2 Hz) than the two studies (e.g., Ekström and Stark (2013)~~  
646 ~~used the frequency band 0.0067 – 0.0286 Hz(35–150 s)). Previous work has shown that, for a~~  
647 ~~given the same event, use of different frequency bands produces landslide force histories of~~  
648 ~~different amplitudes (Hibert et al., 2014; Moore et al., 2017; Zhang et al., 2020b). As a comparison,~~  
649 ~~we performed inversion in the frequency band 0.0067 – 0.0286 Hz, which gave a maximum force~~  
650 ~~of  $1.03 \times 10^{11}$  N and sliding mass estimates of  $4.20 \times 10^{10}$  kg and  $5.60 \times 10^{10}$  kg that are more~~  
651 ~~consistent with our estimation. The newly estimated volumes from empirical relationships are also~~  
652 ~~closer to the DEM-derived volume, accounting for 89% and 119%, respectively. Since the~~

653 frequency bands that we used in the two inversions have similar lower cutoff frequencies. Since  
654 the frequency bands we used are close at the low frequency end, both of which include the duration  
655 of sliding (Gualtieri and Ekström, 2018; Toney and Allstadt, 2021), the kinematic parameters  
656 estimated from both inversion results are essentially similar in their characterization of overall  
657 landslide motion. We used the frequency band including relatively higher frequency energy (up to  
658 0.2 Hz) in the inversion to allow finer scale characteristics of the forces and landslide motion to  
659 be analyzed (Zhao et al., 2015), such as the near-linear increase of the vertical component force in  
660 the first 26 s and subsequent abrupt decrease.

661 ~~from Chao et al. (2016) and Ekström and Stark (2013), are about 1.77 and 1.32 times that~~  
662 ~~derived from pre and post event DEM differencing. This is not surprising as we used a different~~  
663 ~~frequency band in our inversion (0.006–0.2 Hz) than the two studies (e.g., Ekström and Stark (2013)~~  
664 ~~used the period band 35–150 s). Previous work has shown that, for the same event, use of different~~  
665 ~~frequency bands produces landslide force histories of different amplitudes (Hibert et al., 2014;~~  
666 ~~Moore et al., 2017; Zhang et al., 2020b). As a comparison, we performed inversion in the period~~  
667 ~~band 35–150 s, which gave a maximum force of  $1.03 \times 10^{11}$  N and sliding mass estimates of  $5.60$~~   
668  ~~$\times 10^{10}$  kg and  $4.20 \times 10^{10}$  kg that are more consistent with the DEM result. Since the frequency~~  
669 ~~bands we used are close at the low frequency end, the kinematic parameters estimated from both~~  
670 ~~inversion results are essentially similar in their characterization of overall landslide motion. We~~  
671 ~~used the period band including relatively higher frequency energy (up to 0.2 Hz) in the inversion~~  
672 ~~to allow finer scale characteristics of the forces and landslide motion to be analyzed (Zhao et al.,~~

673 ~~2015), such as the near linear increase of the vertical component force in the first 26 s and~~  
674 ~~subsequent abrupt decrease.~~

## 675 **5.2 Link with numerical modeling**

676 The numerical simulation combining signal inversion and field data more realistically reflects  
677 the landslide process than that based on field data alone. Differencing of pre- and post-landslide  
678 terrain data is commonly used to calibrate discrete element simulations; however, it is a recognized  
679 limitation that this method does not inform on whether the landslide process is correctly modeled.  
680 Different combinations of discrete element parameters may produce very similar superposition  
681 results even if the motion processes differ. In this study, the simulation is calibrated by the  
682 accumulation characteristics, and then the landslide movement process is further constrained by  
683 the inversion of the seismic signal. The final simulation results produced CSI of 0.65,  $\delta T_{vmax}$  of  
684 2.5%,  $\delta D_{maxmax}$  of 0.6%,  $\delta T$  of 33.3%,  $\delta V_{max}$  of 33.3% ( $\delta T_{vmax}$ : error of time corresponds to peak  
685 velocity from simulated and inversed;  $\delta D_{max}$ : error of peak displacement from simulated and  
686 inversed;  $\delta T$ : error of time of landslide from simulated and inversed;  $\delta V_{max}$ : error of peak velocity  
687 from simulated and inversed), indicating they reflect the whole process of movement and  
688 accumulation well, overcoming the limitations of traditional methods.

689 Differences in the kinetic characteristics of different landslide phases between the numerical  
690 simulation and inversion are highlighted using analysis of square residue variance (Fig. 12). For  
691 example, the inversion results simulate the sliding stage (0–20\_s) best, the diffusion and  
692 depositionaccumulation stage (40–80\_s) second, and the acceleration stage (20–40\_s) least. The  
693 good simulation of the sliding stage may be due to the fracture zone not yet being completely

694 detached, so landslide movement is dominated by sliding of the whole body, which the theoretical  
695 assumption in the inversion approach. In the acceleration stage of large-scale landslides, friction  
696 between the sliding rock and soil and the base generates heat, which causes thermal compression  
697 and fluidization, leading to soil weakening (Wang et al., 2017, 2018). Reduction in the friction  
698 coefficient means the landslide moves faster, however, this factor is not considered in the current  
699 inversion model, so it ~~overestimates~~under-estimates peak velocity (Fig. 12). Despite the  
700 differences in kinematics, the simulation is essentially consistent with reality in terms of  
701 accumulation and movement characteristics.

### 702 **5.3 Reconstruction of landslide process**

703 The Baige landslide has been the focus of much previous research (Xu et al., 2018; Deng et  
704 al., 2019; Fan et al., 2019a; Ouyang et al., 2019; Zhang et al., 2019; Wang et al., [2020a](#)[2020c](#)),  
705 however, this study is the first analysis that couples seismic signal analysis, dynamic inversion,  
706 and numerical simulation. Our approach of multi-method mutual verification effectively reduces  
707 the inherent ambiguity of each method, and multi-method analysis improves the rationality and  
708 reliability of the results. Based on the characteristics of the “10.10” Baige landslide derived from  
709 our seismic signal inversion and discrete element model simulation analysis, we have developed a  
710 generic model of landslide dynamics (Figure 14). Our findings show the landslide was triggered  
711 by detachment of the weathered layer with severe top fault segmentation and the landslide process  
712 comprised four stages: initiation, main slip, blocking, and deposition, as outlined below.

713 1. Initiation stage (Fig. 14a): The fracture zone on the upper part of the first-level platform  
714 loses stability and slides down under the action of gravity. Landslide debris is hindered by friction

715 on the surface of the main sliding zone, so the landslide body moves relatively slowly. Increasing  
716 debris accumulates on the first-level platform and the lower main sliding area, which increases  
717 instability of the weathered layer, and other debris continues to fall downslope. The surface  
718 weathering layer of the main sliding area starts to slide, and the landslide body forms after the first  
719 fracture in the fracture development zone. Cascading from the initial fracture, continuous  
720 fracturing and sliding of the shear zone causes the landslide body to gradually increase; sliding of  
721 the top surface of the main sliding zone increases the scale of the landslide body. Downward sliding  
722 gradually accelerates as the landslide body increases, but friction in the main sliding area then acts  
723 to decelerate the mass; the deceleration process can be seen in the signal recorded at seismic station  
724 GZI (Fig. 7). As a result, acceleration increases slowly over c. 10 s; this is evident in both the  
725 inversion and numerical simulation results.

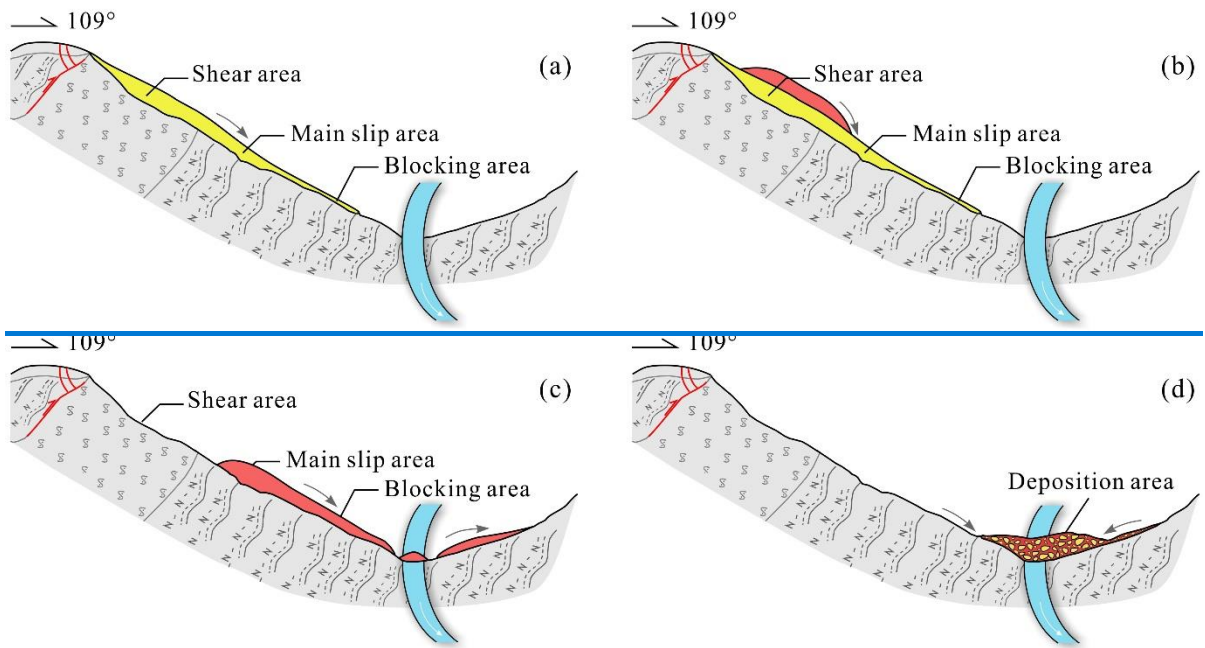
726       2. Main slip stage (Fig. 14b): The main sliding area gradually loses stability and slides rapidly  
727 under the control of structural surfaces formed by weathering; the landslide body passes through  
728 the main sliding area and enters the wide and gentle second level platform where resistance is  
729 relatively high. After crossing the second level platform, the landslide enters the slip resistance  
730 zone where the degree of weathering is relatively weak, so the scouring action of the landslide  
731 body drives resistance. The effect of both sliding and anti-slip zones on the landslide body is  
732 relatively weak and is characterized well by the seismic signal in the time domain and the inverted  
733 acceleration curve. The initial sliding stage of the main sliding zone is reflected in the gradually  
734 increasing acceleration that peaks when the landslide body reaches the second level platform, and  
735 then decreases. When acceleration is approximately zero, the front part of the landslide has entered

736 the river, and velocity of the landslide body peaks; the timing of maximum velocity in the inversion  
737 and simulation is consistent, at 32 s and 34 s, respectively (Fig. 12a).

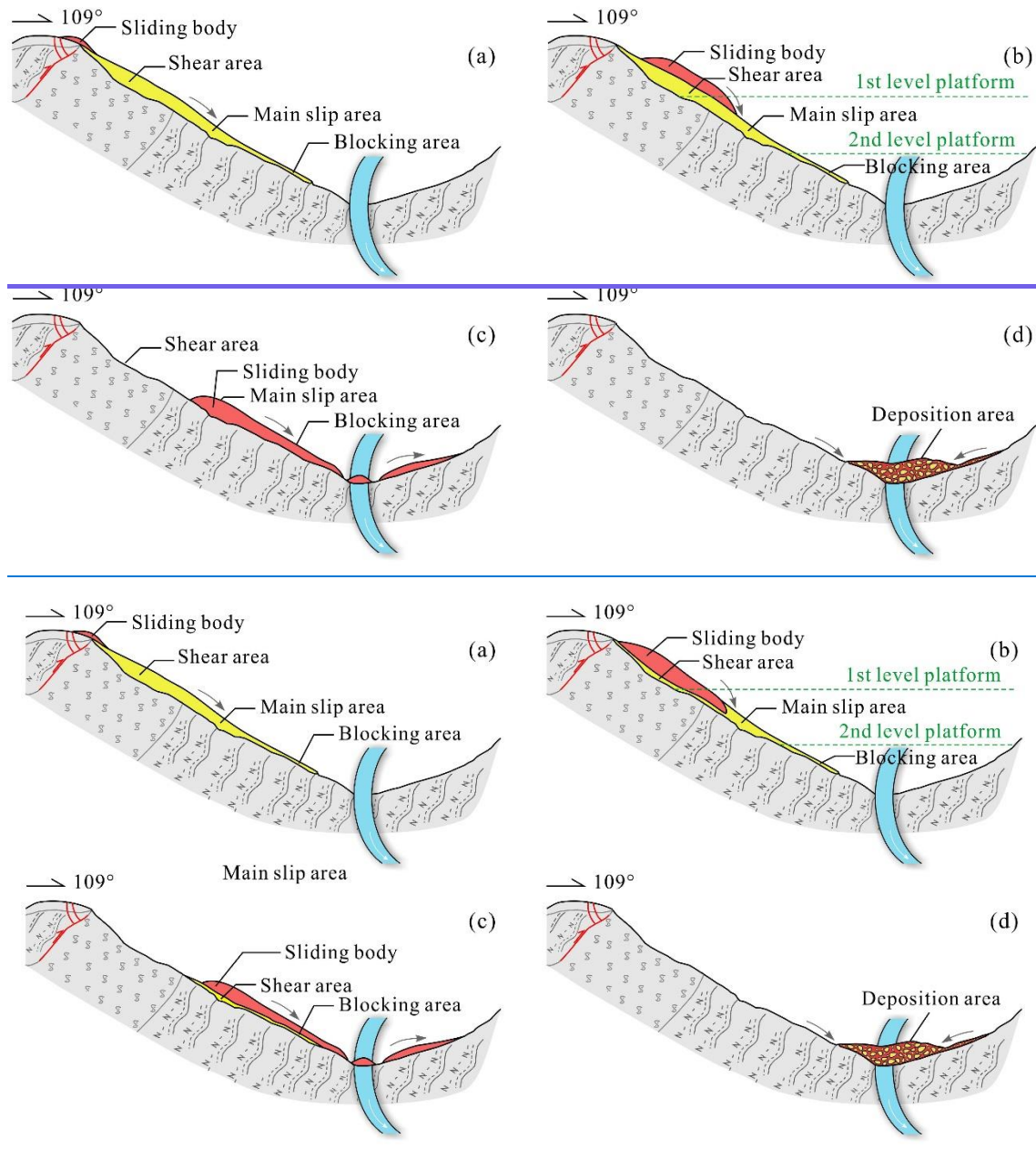
738 3. Blocking stage (Crawling up the opposite valley wall) (Fig. 14c): After passing through the  
739 anti-slip area, the landslide detaches at high speed at an altitude of c. 2950 m and loses support of  
740 the ground surface. Part of the landslide body accumulates in the river and part hits the opposite  
741 (left) bank of the Jinsha River at a high speed and crawls upwards against the valley slope. During  
742 the upward movement, landslide debris spreads upstream and downstream, scouring the left bank  
743 of the river (SA3 in Fig. 1c) and a small area of the right bank (SA4 in Fig. 1c). Landslide debris  
744 reaches a maximum elevation of 3045 m on the opposite slope, then slides downslope under the  
745 action of gravity, forming debris strips like the scratches found on the sliding surface. Some debris  
746 remains on the relatively gentle slope of the left bank. The main feature of this process is that the  
747 action of gravity changes the force of the landslide body from dynamic to resistance; this is well  
748 reflected in the time-domain seismic curve and inversion results (Fig. 8), where the acceleration  
749 switches rapidly from increasing to decreasing over c. 10 s. As the upward crawling situation was  
750 not considered in the model design, the numerical simulation failed to describe the process.

751 4. Deposition stage (Falling back and accumulation) (Fig. 14d): Debris rapidly falls back  
752 down under the action of gravity, colliding with debris in the traction area of the river channel and  
753 interacting with stream flow to form a jet stream. Some finer particles in the landslide body mix  
754 with the sandblasting water to form a water-sand jet that discharges diagonally across the river,  
755 toward the downstream left bank (SA5 in Fig. 1c) and upstream right bank (SA4 in Fig. 1c). Most  
756 of the detrital material stops moving and is deposited in the river channel, forming a barrier dam

757 that starts to pond water. Under gravity and the action of water flow, small fragments at the top of  
758 the dam body lose stability and form a secondary slip zone (SA1 and SA2 in Fig. 1c) that becomes  
759 a drainage channel. The acceleration change during this downturn is roughly the same as the  
760 change trend of the main sliding phase. Acceleration first gradually increases and then decreases  
761 to zero before entering the deceleration phase. The seismic curve in the time domain and the  
762 inverted acceleration curve both characterize this process well, and the inversion results give a  
763 duration of c. 10\_s\_.



764



765

766

767 **Fig. 14.** Schematic diagram of the Baige landslide model. **(a)** Stage 1 – initiation; **(b)** Stage 2 –  
 768 main slip; **(c)** Stage 3 – crawling up against the slope (blocking); **(d)** Stage 4 – falling back and  
 769 accumulation (deposition).

770

## 771 5.4 Research contribution

772 Post-event geological survey can examine depositional characteristics of the landslide and  
 773 weathering and fracture conditions of rocks in the slide source area, which provides some

774 information for understanding landslide causal processes. The seismic signal provides some  
775 information on landslide evolution, with the low-frequency component reflecting the overall  
776 movement trend of the landslide and the high-frequency component reflecting detailed  
777 characteristics of the movement process. Experienced researchers can reconstruct the landslide  
778 process using a combination of geological survey and seismic signal analysis. However, the  
779 propagation effect of the stratum means that the seismic signal does not completely correspond to  
780 landslide movement and may generate false images, as well as confounding precise determination  
781 of landslide start time and duration.

782         Landslide dynamic inversion based on the long-wavelength information of the seismic signal  
783 eliminates the propagation effect which allows the dynamic parameter curve of the landslide to be  
784 obtained, giving a relatively accurate determination of landslide start and end time and event  
785 duration. The dynamic inversion result reflects the change process of the overall movement trend  
786 of the landslide (the low-frequency trend) and can be used to verify the results of combined  
787 geological survey and seismic signal analysis. [The low-frequency \(0~0.2 Hz\) component of](#)  
788 [dynamic parameters, as provided by dynamic inversion, can guide the all band frequency motion,](#)  
789 [constraining the high frequency \(>0.2 Hz\) movement, analysis of the landslide process, which](#)  
790 [helps to reduce ambiguity.](#) ~~The low-frequency component of dynamic parameters, as provided by~~  
791 ~~dynamic inversion, can guide the high-frequency motion analysis of the landslide process, which~~  
792 ~~helps to reduce ambiguity.~~

793         The accuracy of numerical simulation results depends on scientific models and accurate  
794 parameters. When static parameters such as pre- and post-landslide topography are used to select  
795 parameters and constrain results of numerical simulation, there are often multiple solutions. [The](#)  
796 [accuracy of the landslide dynamic with time evolution process will not be determined using only](#)  
797 [the calibration of the depositional morphology, because different velocities, evolutionary processes](#)  
798 [may produce similar accretionary landforms \(An et al. 2021; Mergili et al. 2017\), especially for](#)  
799 [large scale landslides like Baige, which occur next to deep-incised valleys.](#) ~~Dynamic inversion~~  
800 ~~results can dynamically and quantitatively constrain the dynamic parameters and increase the~~

801 ~~credibility of the numerical simulation to produce highly effective simulation of the landslide~~  
802 ~~process. Compared with the study of An et al. (2021), which mainly focuses on force time history~~  
803 ~~inversion, we further added the velocity and displacement characteristics retrieved from seismic~~  
804 ~~signals to conduct dynamic quantitative constraints on dynamic parameters and improve the~~  
805 ~~credibility of numerical simulation, so as to carry out efficient simulation of landslide process.~~ The  
806 improved simulation allows in-depth analysis of frequency motion characteristics of the landslide,  
807 such as speed change, characteristics of each stage, etc. These characteristics can also be used to  
808 verify and optimize the landslide process to improve analysis results.

809 Each of the three methods has disadvantages which may lead to errors and ambiguities in  
810 analyzing landslides. However, the combined use and mutual verification of the different methods  
811 can effectively avoid ambiguity and improve the reasonableness of results.

## 812

## 813 **6. Conclusions**

814 ~~In this study, we used on-site geological survey, landslide seismic signal analysis, dynamic~~  
815 ~~inversion, and numerical simulation to provide a comprehensive analysis of “10.10” Baige~~  
816 ~~landslide. We used short-time Fourier transform (STFT) and PSD to analyze the seismic signals~~  
817 ~~for Baige landslide. We then reconstructed the landslide force history by direct deconvolution of~~  
818 ~~the observed seismograms with Green’s functions. We then developed a method that use seismic~~  
819 ~~inversion to constrain and calibrate the numerical input parameters using DEM. After calibrating~~  
820 ~~the parameters of the numerical models, the dynamic process of the “10.10” Baige landslide was~~  
821 ~~analysed. Nevertheless, several key issues, such as friction coefficient decreases as the landslide~~  
822 ~~progresses, base entrainment, particle breakage, are not considered in the DEM, which leads the~~  
823 ~~difference between simulation and inversion, should be considered in future research.~~The “10.10”  
824 ~~Baige landslide was triggered by instability of highly weathered serpentinite at the top, with severe~~  
825 ~~fracture and cutting, which led to downward sliding of the severely weathered gneiss group in the~~  
826 ~~lower part along the bottom sliding surface. Part of the front edge of the landslide was detached~~  
827 ~~on the bottom of the slip area, blocking area, and some other parts, over the Jinsha Rvier, slid up~~

828 ~~against its opposite slope, and then~~Part of the front edge of the landslide was detached on the left  
829 ~~bank of the Jinsha River, slid up against the opposite slope on the right bank, and then slid down~~  
830 ~~and deposited in the river together with the main landslide body. The accumulated mass blocked~~  
831 ~~the river to impound a barrier lake.~~

832  
833  
834 ~~Our study has demonstrated that combining with on-site geological survey, landslide~~  
835 ~~seismic signal analysis, dynamic inversion, and numerical simulation provides a~~  
836 ~~comprehensive and accurate method for studying the landslide process.~~ On-site geological  
837 ~~survey combined with seismic signal analysis can approximate the overall process of landslide~~  
838 ~~evolution, but the results are influenced by the analyst's experience and professional background,~~  
839 ~~with a relatively high level of training required. Dynamic inversion provides data on changes in~~  
840 ~~dynamic parameters during the landslide process, which enables the analyst to intuitively analyze~~  
841 ~~the physical parameters of the landslide process. However, dynamic inversion results lack the high~~  
842 ~~frequency component of the landslide process; a combination of seismic signal analysis and~~  
843 ~~numerical simulation results is more comprehensive. Dynamic parameter inversion can eliminate~~  
844 ~~the propagation effect of seismic waves and can accurately determine the start and end time of the~~  
845 ~~landslide. The low-frequency changes of dynamic parameters obtained by the inversion inform~~  
846 ~~analysis of the landslide process and calibrate numerical simulation results. Reasonable and~~  
847 ~~accurate numerical simulation results can dynamically visualize the landslide process, which helps~~  
848 ~~in-depth understanding and verification of the landslide process. In short, available methods for~~  
849 ~~landslide analysis each have advantages and disadvantages, but in combination the inherent~~  
850 ~~ambiguities of each method are reduced and the accuracy of landslide process results is increased.~~

## 851 7. Appendix 1

### 852 Macro and Micro Conversion Formula of Discrete Element Model

853 There is an analytical solution between the macro and micromechanical parameters of the  
854 tightly packed discrete element model, that is, the conversion formula proposed by Liu et al. (2013).

855 For the linear elastic model, there are five micromechanical parameters, that is, the normal stiffness  
856 ( $K_n$ ), shear stiffness ( $K_s$ ), breaking displacement ( $X_b$ ), shear resistance ( $F_{s0}$ ), coefficient of friction  
857 ( $\mu_p$ ) can be defined by Young's modulus ( $E$ ), Poisson's ratio ( $\nu$ ), tensile strength ( $T_u$ ), compressive  
858 strength ( $C_u$ ) and coefficient of intrinsic friction ( $\mu_i$ ). The conversion formulas are as follows:

859

$$K_n = \frac{E}{\sqrt{3(1-2\nu)(1+\nu)}} \quad (\text{A1})$$

$$K_s = \frac{E(1-4\nu)}{\sqrt{3(1-2\nu)(1+\nu)}} \quad (\text{A2})$$

$$X_b = \frac{2K_n + K_s}{2\sqrt{3}K_n(K_n + K_s)} T_u d \quad (\text{A3})$$

$$F_{s0} = \left(\frac{1}{4} - \frac{\sqrt{3}}{4} \mu_p\right) C_u d \quad (\text{A4})$$

$$\mu_p = \frac{-3\sqrt{3} + \sqrt{3}I}{3 + 3I}, I = [(1 + \mu_i)^{0.5} + \mu_i]^2 \quad (\text{A5})$$

860

## 861 **7.8. Acknowledgements**

862 This study was financially supported by the National Natural Science Foundation of China  
863 (grant nos. 42120104002, 41901008, U21A2008), the Second Tibetan Plateau Scientific  
864 Expedition and Research Program (STEP) (grant no. 2019QZKK0906), and the Fundamental  
865 Research Funds for the Project of Science & Technology Department of Sichuan Province (grant  
866 no. 2020YFH0085).

867 The probabilistic power spectral densities (PSD) are calculated and plotted using ObsPy  
868 (<https://docs.obspy.org/>).

869

## 870 **Data availability**

871 All raw data can be provided by the corresponding authors upon request.

872

## 873 **Author contributions**

874 The authors of this manuscript entitled “Combining seismic signal dynamic inversion and  
875 numerical modeling improves landslide process reconstruction” are Yan Yan, Yifei Cui, [Jiaojiao](#)  
876 [Zhou](#), Xinghui Huang, Wengang Zhang, Shuyao Yin, ~~[Jiaojiao Zhou](#)~~, [Jian Guo](#), Sheng Hu. Yan Yan  
877 is the first author, is responsible for most of the work and paper writing in this research. Yifei Cui  
878 is the second author and the corresponding author, is responsible for the processing and verification  
879 of the article data. [JiaoJiao Zhou and](#) Xinghui Huang is the third, ~~fourth~~-author and is responsible  
880 for the production of the article figures ~~and tables~~. Wengang Zhang ~~is the fourth author and~~ is  
881 responsible for checking the overall logical structure of the article. Shuyao Yin ~~and Jian Guo~~ is  
882 responsible for the numerical simulations. ~~Jiaojiao Zhou is the seventh author and is responsible~~  
883 ~~for drawing the tables~~. Sheng Hu is responsible for reviewing and editing the manuscript.

884

## 885 **Competing interests**

886 The authors declare that they have no conflict of interest.

887

## 888 **8.9. References**

- 889 Allstadt, K.: Extracting source characteristics and dynamics of the August 2010 Mount M  
890 eager landslide from broadband seismograms, J. Geophys. Res.-Earth, 118, 1472–149  
891 0, <https://doi.org/10.1002/jgrf.20110>, 2013.
- 892 An, H. C., Ouyang, C. J., Zhao, C., and Zhao, W.: Landslide dynamic process and para  
893 meter sensitivity analysis by discrete element method: the case of Turnoff Creek roc  
894 k avalanche, J. Mt. Sci., 17, 1581-1595, <https://doi.org/10.1007/s11629020-5993-7>, 20  
895 20.
- 896 [An, H. C., Ouyang, C. J., Zhou, S.: Dynamic process analysis of the Baige landslide by t  
897 he combination of DEM and long-period seismic waves-, Landslides, 18, 1625-1639,  
898 <https://doi.org/10.1007/s10346-020-01595-0>, 2021.](#)
- 899 Brodsky, E. E., Gordeev, E., and Kanamori, H.: Landslide basal friction as measured by  
900 seismic waves, Geophys. Res. Lett., 30, 2236, <https://doi.org/10.1029/2003GL018485>,  
901 2003.
- 902 Chao, W. A., Zhao, L., Chen, S. C., Wu, Y. M., Chen, C. H., and Huang, H. H.: Seis  
903 mology-based early identification of dam-formation landquake events, Sci. Rep., 6, 1  
904 9259, <https://doi.org/10.1038/srep19259>, 2016.

905 Chao, W. A., Wu, Y. M., Zhao, L., Chen, H., Chen, Y. G., Chang, J. M., and Lin, C.  
906 M.: A first near real-time seismology-based landquake monitoring system, *Sci. Rep.*,  
907 7, 43510, <https://doi.org/10.1038/srep43510>, 2017.

908 Chen, C. H., Chao, W. A., Wu, Y. M., Zhao, L., Chen, Y. G., Ho, W. Y., Lin, T. L.,  
909 Kuo, K. H., and Chang, J. M.: A seismological study of landquakes using a real-ti  
910 me broad-band seismic network, *Geophys. J. Int.*, 194, 885-898, <http://doi.org/10.1093>  
911 /gji/ggt121, 2013.

912 Dahlen, F. A.: Single-force representation of shallow landslide sources, *B. Seismol. Soc.*  
913 *Am.*, 83, 130–143, <http://doi.org/10.1785/BSSA0830010130>, 1993.

914 Dammeier, F., Moore, J. R., Hammer, C., Haslinger, F., and Loew, S.: Automatic detecti  
915 on of alpine rockslides in continuous seismic data using hidden Markov models, *J.*  
916 *Geophys. Res.-Earth*, 121, 351-371, <http://doi.org/10.1002/2015jf003647>, 2016.

917 Darlington, W.J., Ranjith, P.G., and Choi, S.K.: The Effect of Specimen Size on Strength  
918 and Other Properties in Laboratory Testing of Rock and Rock-Like Cementitious Br  
919 ittle Materials, *Rock Mech Rock Eng.*, 44, 513, <https://doi.org/10.1007/s00603-011-016>  
920 1-6, 2011.

921 Deng, J. J., Gao, Y. J., Yu, Z. Q., and Xie, H. P.: Analysis on the Formation Mechanis  
922 m and Process of Baige Landslides Damming the Upper Reach of Jinsha River, Chin  
923 a, *Adv. Eng. Sci.*, 51, 9-16, <http://doi.org/10.15961/j.jsuese.201801438>, 2019.(In Chine  
924 se)

925 Ekström, G., and Stark, C. P.: Simple scaling of catastrophic landslide dynamics, *Science*.  
926 339, 1416–1419. <https://doi.org/10.1126/science.1232887>, 2013.

927 Fan, X., Yang, F., Subramanian, S. S., Xu, Q., Feng, Z., Mavrouli, O., Peng, M., Ouyan  
928 g, C., Jansen, D., and Huang, R.: Prediction of a multi-hazard chain by an integrate  
929 d numerical simulation approach: the Baige landslide, Jinsha River, China, *Landslide*  
930 *s*, 17, 147-164, <http://doi.org/10.1007/s10346-019-01313-5>, 2019a.

931 Fan, X., Xu, Q., Liu, J., Subramanian, S. S., He, C., Zhu, X., and Zhou, L.: Successful  
932 early warning and emergency response of a disastrous rockslide in Guizhou province,  
933 China, *Landslides*, 16, 2445–2457, <https://doi.org/10.1007/s10346-019-01269-6>, 2019b.

934 Favreau, P., Mangeney, A., Lucas, A., Crosta, G., and Bouchut, F.: Numerical modeling  
935 of landquakes, *Geophys. Res. Lett.*, 37, L15305, <http://doi.org/10.1029/2010gl043512>,  
936 2010.

937 Feng, Z.: The seismic signatures of the 2009 Shiaolin landslide in Taiwan, *Nat. Hazards*  
938 *Earth Syst. Sci.*, 11, 1559-1569, <http://doi.org/10.5194/nhess-11-1559-2011>, 2011.

939 Feng, Z. Y., Lo, C. M., and Lin, Q. F.: The characteristics of the seismic signals induce  
940 d by landslides using a coupling of discrete element and finite difference methods,  
941 *Landslides*, 14, 661-674, <http://doi.org/10.1007/s10346-016-0714-6>, 2016.

942 Froude, M. J., and Petley, D. N.: Global fatal landslide occurrence from 2004 to 2016,  
943 *Nat. Hazards Earth Syst. Sci.*, 18, 2161-2181, <http://doi.org/10.5194/nhess-18-2161-201>  
944 8, 2018.

945 Fuchs, F., Lenhardt, W., and Bokelmann, G.: Seismic detection of rockslides at regional  
946 scale: examples from the Eastern Alps and feasibility of kurtosis-based event locatio  
947 n, *Earth Surf. Dynam.*, 6, 955-970, <http://doi.org/10.5194/esurf-6-955-2018>, 2018.

948 Fukao, Y.: Single-force representation of earthquakes due to landslides or the collapse of  
949 caverns, *Geophys. J. Int.*, 122, 243–248, <https://doi.org/10.1111/j.1365-246X.1995.tb03>  
950 551.x, 1995.

951 Gualtieri, L., and Ekström, G.: Broad-band seismic analysis and modeling of the 2015 T  
952 aan Fjord, Alaska landslide using Instaseis, *Geophys. J. Int.*, 213, 1912–1923, <https://>  
953 <doi.org/10.1093/gji/ggy086>, 2018.

954 Hasegawa, H. S., and Kanamori, H.: Source mechanism of the magnitude 7.2 Grand Ban  
955 ks earthquake of November 1929: Double couple or submarine landslide?, *B. Seismo*  
956 *l. Soc. Am.*, 77, 1984–2004, 1987.

957 Helmstetter, A., and Garambois, S.: Seismic monitoring of Séchilienne rockslide (French  
958 Alps): Analysis of seismic signals and their correlation with rainfall, *J. Geophys. Re*  
959 *s.*, 115, F03016, <http://doi.org/10.1029/2009jf001532>, 2010.

960 [Hencher, S. R., Richards, L. R.: Assessing the Shear Strength of Rock Discontinuities at](https://doi.org/10.1007/s00603-014-0633-6)  
961 [Laboratory and Field Scales, \*Rock Mech Rock Eng.\*, 48, 883-905, <https://doi.org/10.1>](https://doi.org/10.1007/s00603-014-0633-6)  
962 [007/s00603-014-0633-6](https://doi.org/10.1007/s00603-014-0633-6), 2014.

963 Hibert, C., Ekström, G., and Stark, C. P.: Dynamics of the Bingham Canyon Mine lands  
964 lides from seismic signal analysis, *Geophys. Res. Lett.*, 41, 4535–4541, <https://doi.org>  
965 [/10.1002/2014GL060592](https://doi.org/10.1002/2014GL060592), 2014.

966 Hibert, C., Stark, C. P., and Ekström, G.: Dynamics of the Oso-Steelhead landslide from  
967 broadband seismic analysis, *Nat. Hazards Earth Syst. Sci.*, 15, 1265–1273, [https://doi.](https://doi.org)  
968 [org/10.5194/nhess-15-1265-2015](https://doi.org/10.5194/nhess-15-1265-2015), 2015.

969 [Hoek E.: Rock engineering course notes by Evert Hoek. <http://www.rocscience.com/educat>](http://www.rocscience.com/education/hoek-corner)  
970 [ion/hoek's corner, 2000.](http://www.rocscience.com/education/hoek-corner)

971 Jiang, Y., Wang, G., and Kamai, T.: Fast shear behavior of granular materials in ring-sh  
972 ear tests and implications for rapid landslides, *Acta Geotech.*, 12, 645-655, [http://doi.](http://doi.org)  
973 [org/10.1007/s11440-016-0508-y](http://doi.org/10.1007/s11440-016-0508-y), 2016.

974 Kääh, A., Leinss, S., Gilbert, A., Bühler, Y., Gascoin, S., Evans, S. G., Bartelt, P., Bert  
975 hier, E., Brun, F., Chao, W. A., Farinotti, D., Gimbert, F., Guo, W., Huggel, C., Ka  
976 rgel, J.S., Leonard, G.J., Tian, L., Treichler, D., and Yao, T.: Massive collapse of t  
977 wo glaciers in western Tibet in 2016 after surge-like instability, *Nat. Geosci.*, 11, 11  
978 4–120, <https://doi.org/10.1038/s41561-017-0039-7>, 2018.

979 Kanamori, H., and Given, J.W.: Analysis of long-period seismic waves excited by the M  
980 ay 18, 1980, eruption of Mount St. Helens—A terrestrial monopole?, *J. Geophys. Re*  
981 *s.-Sol. Ea.*, 87, 5422–5432, <https://doi.org/10.1029/JB087iB07p05422>, 1982.

982 Kanamori, H., Given, J. W., and Lay, T.: Analysis of seismic body waves excited by th  
983 e Mount St. Helens eruption of May 18, 1980, *J. Geophys. Res.-Sol. Ea.*, 89, 1856–  
984 1866, <https://doi.org/10.1029/JB089iB03p01856>, 1984.

985 Kao, H., Kan, C. W., Chen, R. Y., Chang, C. H., Rosenberger, A., Shin, T. C., Leu, P.  
986 L., Kuo, K. W., and Liang, W. T.: Locating, monitoring, and characterizing typhoon  
987 -induced landslides with real-time seismic signals, *Landslides*, 9, 557-563, <http://doi.org/10.1007/s10346-012-0322-z>, 2012.

989 Li, C. Y., Wang, X. C., He, C. Z., Wu, X., Kong, Z. Y., and Li, X. L. China National  
990 Digital Geological Map (Public Version at 1:200 000 Scale) Spatial Database(V1). D  
991 evelopment and Research Center of China Geological Survey; China Geological Surv  
992 ey[producer], 1957. National Geological Archives of China [distributor], 2019-06-30.  
993 <https://doi.org/10.23650/data.A.2019.NGA120157.K1.1.1.V1>, 2019a.

994 Li, W., Chen, Y., Liu, F., Yang, H., Liu, J., and Fu, B.: Chain-style landslide hazardous  
995 process: Constraints from seismic signals analysis of the 2017 Xinmo landslide, SW  
996 China, *J. Geophys. Res.-Sol. Ea.*, 124, 2025–2037, [https://doi.org/10.1029/2018JB0164](https://doi.org/10.1029/2018JB016433)  
997 33, 2019b.

998 Li, Z., Huang, X., Xu, Q., Yu, D., Fan, J., and Qiao, X.: Dynamics of the Wulong land  
999 slide revealed by broadband seismic records, *Earth, Planets Space*, 69, 27, <https://doi.org/10.1186/s40623-017-0610-x>, 2017.

1001 Li, Z., Huang, X., Yu, D., Su, J., and Xu, Q.: Broadband-seismic analysis of a massive  
1002 landslide in southwestern China: Dynamics and fragmentation implications, *Geomorph*  
1003 *ology*, 336, 31–39. <https://doi.org/10.1016/j.geomorph.2019.03.024>, 2019c.

1004 Liu, C., Pollard, D. D., and Shi, B.: Analytical solutions and numerical tests of elastic a  
1005 nd failure behaviors of close-packed lattice for brittle rocks and crystals, *J. Geophys.*  
1006 *Res.-Sol. Ea.*, 118, 71-82, <https://doi.org/10.1029/2012JB009615>, 2013.

1007 Liu, C., Xu, Q., Shi, B., Deng, S., and Zhu, H.: Mechanical properties and energy conve  
1008 rsion of 3D close-packed lattice model for brittle rocks, *Comput. Geosci.*, 103, 12-20,  
1009 <https://doi.org/10.1016/j.cageo.2017.03.00>, 2017.

1010 [Liu, C., Fan, X., Zhu, C., and Shi, B.: Discrete element modeling and simulation of 3-D](#)  
1011 [imensional large-scale landslide-Taking Xinmocun landslide as an example-, \*J. Eng.\*](#)  
1012 [Geol, 27, 1362-1370-, <https://doi.org/10.13544/j.cnki.jeg.2018-234>, 2019. \(In Chinese\)](#)

1013 Lo, C. M., Lin, M. L., Tang, C. L., and Hu, J. C.: A kinematic model of the Hsiaolin  
1014 landslide calibrated to the morphology of the landslide deposit, *Eng. Geol.*, 123, 22-  
1015 39, <https://doi.org/10.1016/j.enggeo.2011.07.002>, 2011.

1016 [McNamara, D.E., Buland, R.P., 2004. Ambient Noise Levels in the Continental United St](#)  
1017 [ates. \*Bull. Seismol. Soc. Am.\* 94, 1517–1527. <https://doi.org/10.1785/012003001>](#)

1018

1019 Mergili, M., Fischer, J. T., Krenn, J., and Pudasaini, S. P.: r. avaflow v1, an advanced o  
1020 pen-source computational framework for the propagation and interaction of two-phase  
1021 mass flows, *Geosci. Model Dev*, 10, 553-569, [https://doi.org/10.5194/gmd-10-553-201](https://doi.org/10.5194/gmd-10-553-2017)  
1022 7, 2017.

1023 [Mergili, M., Emmer, A., Juřicová A., Cochachin, A., Fischer, J. T., Huggel, C., and Pud](#)  
1024 [asaini, S. P.: How well can we simulate complex hydro-geomorphic process chains?](#)

1025 [The 2012 multi-lake outburst flood in the Santa Cruz Valley \(Cordillera Blanca, Per](#)  
1026 [ú\), \*Earth Surf Process Landf\*, 43, 1373-1389, <https://doi.org/10.1002/esp.4318>, 2017.](#)

1027 Moore, J. R., Pankow, K. L., Ford, S. R., Koper, K. D., Hale, J. M., Aaron, J., and Lar  
1028 sen, C.F.: Dynamics of the Bingham Canyon rock avalanches (Utah, USA) resolved  
1029 from topographic, seismic, and infrasound data, *J. Geophys. Res.-Earth*, 122, 615–64  
1030 0, <https://doi.org/10.1002/2016JF004036>, 2017.

1031 Moretti, L., Mangeney, A., Capdeville, Y., Stutzmann, E., Huggel, C., Schneider, D., and  
1032 Bouchut, F.: Numerical modeling of the Mount Steller landslide flow history and of  
1033 the generated long period seismic waves, *Geophys. Res. Lett.*, 39, L16402, <https://doi.org/10.1029/2012GL052511>, 2012.

1035 Moretti, L., Allstadt, K., Mangeney, A., Capdeville, Y., Stutzmann, E., and Bouchut, F.:  
1036 Numerical modeling of the Mount Meager landslide constrained by its force history  
1037 derived from seismic data, *J. Geophys. Res.-Sol. Ea.*, 120, 2579–2599, <https://doi.org/10.1002/2014JB011426>, 2015.

1039 Muceku, Y., Korini, O., and Kuriqi, A.: Geotechnical analysis of hill's slopes areas in h  
1040 eritage town of Berati, Albania. *Period. Polytech., Civ. Eng.* 60, 61-73, <https://doi.org/10.3311/PPci.7752>, 2016.

1042 Ouyang, C. J., An, H. C., Zhou, S., Wang, Z. W., Su, P. C., and Wang, D. P.: Insights  
1043 from the failure and dynamic characteristics of two sequential landslides at Baige v  
1044 illage along the Jinsha River, China, *Landslides*, 16, 1397-1414, <https://doi.org/10.1007/s10346-019-01177-9>, 2019.

1046 Pastor, M., Blanc, T., Haddad, B., Petrone, S., Sanchez, M. M., Drempevic, V., Issler, D.,  
1047 Crosta, G. B., Cascini, L., Sorbino, G., and Cuomo, S.: Application of a SPH dept  
1048 hintegated model to landslide run-out analysis, *Landslides*, 11, 793812, <https://doi.org/10.1007/s10346-014-0484-y>, 2014.

1050 [Peterson, J.R., 1993. Observations and modeling of seismic background noise, U.S. Geolo](#)  
1051 [gical Survey Open-File Report 93-322. <https://doi.org/10.3133/ofr93322>.](#)

1052 Pitman, E. B., Nichita, C. C., Patra, A., Bauer, A., Sheridan, M., and Bursik, M.: Comp  
1053 uting granular avalanches and landslides, *Phys. Fluids.*, 15, 3638-3646, <https://doi.org/10.1063/1.1614253>, 2003.

1055

1056 Sakals, M. E., Geertsema, M., Schwab, J. W., and Foord, V. N.: The Todagin Creek lan  
1057 dslide of October 3, 2006, Northwest British Columbia, Canada, *Landslides*, 9, 107-1  
1058 15, <http://doi.org/10.1007/s10346-011-0273-9>, 2011.

1059 Schöpa, A., Chao, W. A., Lipovsky, B. P., Hovius, N., White, R. S., Green, R. G., and  
1060 Turowski, J. M.: Dynamics of the Askja caldera July 2014 landslide, Iceland, from  
1061 seismic signal analysis: precursor, motion and aftermath, *Earth Surf. Dynam.*, 6, 467  
1062 –485, <https://doi.org/10.5194/esurf-6-467-2018>, 2018.

1063 Shen, W., Li, T., Li, P., and Lei, Y.: Numerical assessment for the efficiencies of check  
1064 dams in debris flow gullies: A case study, *Comput. Geotech.*, 122, 103541, <https://doi.org/10.1016/j.compgeo.2020.103541>, 2020.

1065

1066 Sheng, M., Chu, R., Wang, Y., and Wang, Q.: Inversion of source mechanisms for single-force events using broadband waveforms, *Seismol. Res. Lett.*, 91, 1820–1830, <https://doi.org/10.1785/0220190349>, 2020.

1067  
1068

1069 Soga, K., Alonso, E., Yerro, A., Kumar, K., and Bandara, S.: Trends in large-deformation analysis of landslide mass movements with particular emphasis on the material point method, *Géotechnique*, 66, 1-26, <https://doi.org/10.1680/jgeot.15.lm.005>, 2016.

1070  
1071

1072 [Toney, L., Allstadt, K.E.: Isforce: A Python-Based Single-Force Seismic Inversion Framework for Massive Landslides. \*Seismol. Res. Lett.\* 92, 2610–2626. <https://doi.org/10.1785/0220210004>, 2021.](#)

1073  
1074

1075 Walter, M., Arnhardt, C., and Joswig, M.: Seismic monitoring of rockfalls, slide quakes, and fissure development at the Super-Sauze mudslide, French Alps, *Eng. Geol.*, 128, 12-22, <http://doi.org/10.1016/j.enggeo.2011.11.002>, 2012.

1076  
1077

1078 Wang, L. Q., Yin, Y. P., Huang, B. L., and Dai, Z. W.: Damage evolution and stability analysis of the Jianchuandong Dangerous Rock Mass in the Three Gorges Reservoir Area, *Eng. Geol.*, 265, 105439, <http://dx.doi.org/10.1016/j.enggeo.2019.105439>, 2020a.

1079  
1080

1081 Wang, L., Wu, C. Z., Gu, X., Liu, H. L., Mei, G. X., and Zhang, W. G.: Probabilistic stability analysis of earth dam slope under transient seepage using multivariate adaptive regression splines, *Bull. Eng. Geol. Environ.*, 79, 2763–2775, <http://dx.doi.org/10.1007/s10064-020-01730-0>, 2020b.

1082  
1083  
1084

1085 Wang, R.: A simple orthonormalization method for stable and efficient computation of Green's functions, *B. Seismol. Soc. Am.*, 89, 733–741, 1999.

1086

1087 Wang, W., Yin, Y., Zhu, S., Wang, L., Zhang, N., and Zhao, R.: Investigation and numerical modeling of the overloading-induced catastrophic rockslide avalanche in Baige, Tibet, China, *Bull. Eng. Geol. Environ.*, 79, 1765-1779, <https://doi.org/10.1007/s10064-019-01664-2>, 2020c.

1088  
1089  
1090

1091 Wang, Y. F., Dong, J. J., Cheng, Q. G.: Velocity-dependent frictional weakening of large rock avalanche basal facies: Implications for rock avalanche hypermobility?, *J. Geophys. Res.-Sol. Ea.*, 122, 1648-1676, <https://doi.org/10.1002/2016JB013624>, 2017.

1092  
1093

1094 Wang, Y. F., Dong, J. J., Cheng, Q. G.: Normal stress-dependent frictional weakening of large rock avalanche basal facies: Implications for the rock avalanche volume effect, *J. Geophys. Res.-Sol. Ea.*, 123, 3270-3282, <https://doi.org/10.1002/2018JB015602>, 2018.

1095  
1096  
1097

1098 Xu, Q., Zheng, G., Li, W. L., He, C. Y., Dong, X. J., Guo, C., and Feng, W. K.: Study on Successive Landslide Damming Events of Jinsha River in Baige Village on October 11 and November 3, 2018, *J. Eng. Geo*, 26, 1534-1551, <https://doi.org/10.13544/j.cnki.jeg.2018-406>, 2018. (In Chinese)

1099  
1100

1101 Yamada, M., Matsushi, Y., Chigira, M., Mori, J.: Seismic recordings of landslides caused by Typhoon Talas (2011), Japan, *Geophys. Res. Lett.*, 39, L13301, <http://doi.org/10.1029/2012gl052174>, 2012.

1102  
1103  
1104

1105 Yamada, M., Kumagai, H., Matsushi, Y., and Matsuzawa, T.: Dynamic landslide processes revealed by broadband seismic records, *Geophys. Res. Lett.*, 40, 2998–3002, <https://doi.org/10.1002/grl.50437>, 2013.

1108 Yamada, M., Mangeney, A., Matsushi, Y., and Moretti, L.: Estimation of dynamic friction of the Akatani landslide from seismic waveform inversion and numerical simulation, *Geophys. J. Int.*, 206, 1479–1486. <https://doi.org/10.1093/gji/ggw216>, 2016.

1111 Yamada, M., Mangeney, A., Matsushi, Y., and Matsuzawa, T.: Estimation of dynamic friction and movement history of large landslides, *Landslides*, 15, 1963–1974, <https://doi.org/10.1007/s10346-018-1002-4>, 2018.

1114 Yan, Y., Cui, Y., Guo, J., Hu, S., Wang, Z., and Yin, S.: Landslide reconstruction using seismic signal characteristics and numerical simulations: Case study of the 2017 “6.24” Xinmo landslide, *Eng. Geol.*, 270, 105582, <http://doi.org/10.1016/j.enggeo.2020.105582>, 2020a.

1118 Yan, Y., Cui, Y., Tian, X., Hu, S., Guo, J., Wang, Z., Yin, S., and Liao, L.: Seismic signal recognition and interpretation of the 2019 “7.23” Shuicheng landslide by seismogram stations, *Landslides*, 17, 1191-1206, <http://doi.org/10.1007/s10346-020-01358-x>, 2020b.

1122 [Yan, Yan., Yifei, Cui., Dingzhu, Liu., Hui, Tang., Yongjian, Li., Xin, Tian., Lei, Zhang., and Sheng, Hu.: Seismic Signal Characteristics and Interpretation of the 2020 “6.17” Danba Landslide Dam Failure Hazard Chain Process , \*Landslides\*, 18\(6\): 2175-2192. <https://doi.org/10.1007/s10346-021-01657-x>, 2021.](#)

1126 Yu, D., Huang, X., and Li, Z.: Variation patterns of landslide basal friction revealed from long-period seismic waveform inversion, *Nat. Hazards*, 100, 313–327, <https://doi.org/10.1007/s11069-019-03813-y>, 2020.

1129 [Zhang, L., Xiao, T., He, J., and Chen, C.: Erosion-based analysis of breaching of Baige landslide dams on the Jinsha River, China, in 2018, \*Landslides\*, 16, 1965-1979, <http://doi.org/10.1007/s10346-019-01247-y>, 2019.](#)

1132 Zhang, S. L., Yin, Y. P., Hu, X. W., Wang, W. P., Zhang, N., Zhu, S. N., and Wang, L. Q.: Dynamics and emplacement mechanisms of the successive Baige landslides on the Upper Reaches of the Jinsha River, China, *Eng. Geol.*, 278, 105819, <http://dx.doi.org/10.1016/j.enggeo.2020.105819>, 2020a.

1136 Zhang, Z., He, S., Liu, W., Liang, H., Yan, S., Deng, Y., Bai, X., and Chen, Z.: Source characteristics and dynamics of the October 2018 Baige landslide revealed by broadband seismograms, *Landslides*, 16, 777-785, <http://doi.org/10.1007/s10346-019-01145-3>, 2019.

1140 Zhang, Z., He, S., and Li, Q.: Analyzing high-frequency seismic signals generated during a landslide using source discrepancies between two landslides, *Eng. Geol.*, 272, 105640, <https://doi.org/10.1016/j.enggeo.2020.105640>, 2020b.

1143 Zhao, J., Moretti, L., Mangeney, A., Stutzmann, E., Kanamori, H., Capdeville, Y., Calder, E. S., Hibert, C., Smith, P. J., Cole, P., and Lefriant, A.: Model space exploration

1145 for determining landslide source history from long-period seismic data, *Pure Appl. G*  
1146 *eophys.*, 172, 389–413, <https://doi.org/10.1007/s00024-014-0852-5>, 2015.

1147 Zhao, J., Ouyang, C. J., Ni, S. D., Chu, R. S., and Mangeney, A.: Analysis of the 2017  
1148 June Maoxian landslide processes with force histories from seismological inversion  
1149 and terrain features, *Geophys. J. Int.*, 222, 1965–1976, <https://doi.org/10.1093/gji/ggaa>  
1150 226, 2020.

1151 Zhou, L., Fan, X., Xu, Q., Yang, F., and Gou, C.: Numerical simulation and hazard pre  
1152 diction on movement process characteristics of Baige landslide in Jinsha river, *Eng.*  
1153 *Geol.*, 27, 1395-1404, <https://doi.org/10.13544/j.cnki.jeg.2019-037>, 2019. (In Chines  
1154 e)